Mesoscopic simulation of heat conduction in randomly packed beds through lattice-based computation and realistic particle reconstruction

Mingzhi Wang[a,b,c], Chaoyang Shang[a,b,c], Liang Li[a,b,c], Xu Yang[a,b,c]*, Wei Zhao [a,b,c], Abir Al-Tabbaa[d]

[a] Key Lab of Structures Dynamic Behavior and Control of the Ministry of Education, Harbin Institute of Technology, Harbin, 150090, CN

[b] Key Lab of Smart Prevention and Mitigation of Civil Engineering Disasters of the Ministry of Industry and Information Technology, Harbin Institute of Technology, Harbin, 150090, CN

[c] School of Civil Engineering, Harbin Institute of Technology, Harbin, 150090, CN

[d] Department of Engineering, University of Cambridge, Trumpington Street, Cambridge, CB2 1PZ, UK

*Corresponding author. Corresponding author. School of Civil Engineering, Harbin Institute of Technology, Harbin, 150090, CN.

E-mail address: yangxu_civileng@hit.edu.cn (X. Yang); mwang@hit.edu.cn (M. Wang)

Keywords

Packed beds; Lattice-based computation; Heat transfer; Mathematical simulation; Energy; Numerical analysis.

Abstract

Packed beds are heterogeneous media inspiring the design of novel thermal devices. The heterogeneity leads to the anisotropic heat transfer behaviour, which raises the complexity of the analysis and design process. This paper presents an originally developed framework for the computation of heat conduction behaviour in packed beds. The formation of the packing structures was realised with practical rock data. The core computation adopted a three-dimensional lattice-based algorithm. Several digital tests were introduced, including temperature tracking, energy-tracking, round-trip efficiency and heat flux distribution. It was found that the random close packing of natural rocks can maintain a relatively stable heat release and storage performance in the representative volume. An increment of the solid phase fraction does not always enhance the heat release and storage performance, and there exists a threshold between 34.93% and 42.33% solid phase fraction to trigger the positive correlation. A decrease in the solid phase fraction improves the heat intake efficiency but reduces the temperature maintenance performance. The critical time threshold for balanced round-trip efficiency is located at around 13.89 lattice hours without additional thermal interference. Energy round-trip efficiency is an intrinsic property of the packed structure. It was statistically found that the power function is highly likely to be the energy evolution function from upscaling characterisation. The generalised logistic function can provide a fitting recovery of the heat flux distribution from downscaling characterisation. The developed computational framework demonstrates a feasible

bottom-up routine for thermal device design and heat transfer analysis.

1.0 Introduction

Packed beds are a special form of porous media for heat storage and exchange [1,2]. Unlike most types of porous media in wet environments, such as cement and pollution sorbents, the pore structure in packed beds can serve as a heat transfer path in both wet and dry environments [3,4]. In engineering practice, packed beds have been thermally applied in air-conditioning [5], infrastructure functionalization [6], solar energy conversion [7], combustion control [7], geothermal reservoirs [8], etc. The feature of using natural materials as components and the adaptability for clean energy make packed beds an environmentally friendly thermal medium [9] in the background of the energy crisis [10] and climate change [11]. Although applications of packed beds emerged as a result of the above merit, the thermal design and analysis process still faces challenges [12]. One of the challenges is the mathematical description of the random boundaries originating from the packing with irregular particles in practice [13]. The economic advantage of thermal packed beds benefits from naturally obtained materials such as rock, sand and soil [14–16]. Those materials inevitably have irregular shapes involved in the packing process. Another noticeable challenge is the thermal performance evaluation under heterogeneous conditions [17]. The advanced thermal properties of the packed bed are enabled by the multi-phase composite, which can be preliminarily categorised into the solid phase and pore phase. The pore phase performs external mass transfer with environmental air, and the solid phase performs heat exchange with the internally adjacent pore phase [18]. Hence, adopting a homogeneous assumption for the thermal performance evaluation is against the characteristics of packed beds. Progress in the above two problems is essential to developing a designable routine before massive construction and adoption of packed beds as common heat control infrastructures.

The essential requirement for a packed bed model is the numerical recovery of a realistic packing structure with irregular-shaped particles. The solution for this problem mostly relies on the particle packing simulation [19]. The particle packing formation modelling, also known as the jamming issue [20], has been studied both experimentally and numerically for decades [21,22]. It was experimentally observed that the random packing of monosized smooth spherical particles can reach the highest random close packing (RCP) density of 0.64 [23], which is always smaller than the virtual face-centred cubic packing density of 0.74 [24]. Because of the existence of resistance, such as macroscopic friction and microscopic van der Waals force, realistic particle packing density is always smaller than the RCP density[25,26]. The investigation into the stable pore structure with the lowest packing density led to the concept of random loose packing (RLP) [27]. The friction-controlled RLP density was reported to be 0.55 [28], but fixed RLP density values do not exist since certain force systems can provide stable levitation [29]. Putting aside the tone of ‘RCP or RLP was ill-defined’, several algorithms were constructively developed to build mathematical descriptions of the packing structure. Random sequential addition (RSA) is one of the earliest ones, which still functions well as a preliminary modelling algorithm due to its computational efficiency [30,31]. Although RSA provided invaluable inspiration for porous media modelling methodology, the highest packing density from RSA is always lower than

the above-mentioned RLP density [32]. To overcome the limitation of low particle phase fraction, a particle growth algorithm (PGA) was developed based on the initial condition provided by point-based RSA [33]. The proposal of PGA demonstrated that the jamming can be numerically realised without dynamic analysis. However, the control of particle size in PGA limited its realistic correspondence. Almost in the same period, the discrete element method (DEM) solution [34] emerged to model the macroscopic particle packing processes, adopting a similar routine as the molecular dynamics (MD) solution for condensed matter [35]. The high degrees of freedom force system at the macroscopic level is much different from the molecular level and astrophysics level, hence a significant contribution has been made to complete the physics of particle interaction in civil practice. The analytic geometry basis of DEM and MD requires analytic geometry equations to locate the particles. The shape equations in DEM are still being extended to include ellipsoids [36], cylinders [37], cubes [38], etc. However, the well-established spherical routine cannot be directly imported into non-spherical shaped particles, leading to a significant algorithm modification requirement for each specific shape equation [39]. On the other hand, modelling irregularly shaped particles as a composite of spheres appears to be one feasible solution for packing with arbitrarily shaped particles [40,41]. This thought can be generalised as constructing complex shapes with basic geometrical units of spheres. The branch of dynamics-less modelling still had its inheritance, in which a random walk algorithm successfully realised loose packing with strict control of particle sizes [42]. Although the peak packing density for monosized spheres was still not realised, the algorithm demonstrated a strong capability for arbitrarily shaped particles due to its lattice-based design. More recently, the abovementioned algorithm was further coupled with contact mechanics and validated with RCP density [43]. The three-dimensional algorithm still has the merit of arbitrary shape capability, in which the supportive design was representing certain particles with basic geometrical units of voxels [44].

The continuum thermal dynamics theory has an even longer history of development for heat transfer [45]. The Fourier law of heat conduction performs an essential role in calculating the heat flux distribution from the spatial temperature difference, which further enables the estimation of the temperature change rate if heat capacity is available [46]. The complexity of packed beds raises the challenge and possibility of providing thermal characterisation for design and analysis, both numerically and experimentally. By designing a proper thermal device, the bulk performance of thermal transfer in a cubic domain was investigated through an experimental approach [47]. An attempt to investigate the local heat transfer of packed beds with regular particle arrangement was conducted in a cylindrical device [48]. Although the experimental techniques have improved significantly in recent times, it is still extremely difficult to capture coordinate-level heat flux and extract the individual influence from certain heat transfer types. Hence, numerical modelling is necessary to obtain a comprehensive understanding of the transfer behaviour within the porous media of a thermal device. A top-down approach with the homogenous assumption is a convenient path to roughly estimate the heat transfer behaviour in the packed beds. Regression of the experimental data from thermal property development can be induced into an empirical model [49]. Existing empirical models and constitutive models in the form of equations can provide a thermal estimation of intrinsic properties such as conductivity [50] and extrinsic

appearance such as temperature [51]. Attempts for pure mathematical modelling through a top-down approach in a non-differential equations form can illustrate the correlation between certain thermal parameters and non-thermal parameters [52]. The above-mentioned top-down models fundamentally simplified the thermal behaviour by considering the porous media as a bulk volume or area [53]. However, applicable packed beds in practical infrastructure inevitably require a design with material-level understanding before a massive investment. Hence, the bottom-up approach with the heterogeneous assumption is of great significance for the numerical development of the packed beds. Spherical packed beds [54] with non-random placement help the preliminary construction of the heterogeneous geometry for mass transfer in a packed bed with the Lattice Boltzmann method (LBM) [55]. The same methodology of non-random placement of spherical particles was directly adopted in the analysis of constitutive heat transfer in regularly packed beds in 2D [56] and 3D [57]. On the other hand, naturally formed packed beds always have random packing configurations with irregular-shaped particles. The feature of random packing brings the necessity to combine the previously mentioned packing algorithm with the modelling for heat and mass transfer. The mono-size sphere simplification was adopted in randomly packed beds to model the heat transfer in 2D [58] and 3D [59]. On the algorithm aspect, DEM is currently popular in the construction of random packing structures [59,60]. Nevertheless, solutions with other methods to realise irregular particle packing still have a huge open discussion space for methodology development. One solid solution is the direct use of 3D X-ray computed tomography images of the practical packing rocks [61]. Additionally, a hint was provided in a previous contribution for 2D random packing with voxel units [62]. Beyond the algorithm development, the upscale energy performance of a thermal device with a packed bed needs to be introduced as post-processing from the application end [63–67].

In this study, we developed a modelling framework of heat conduction through packed beds constructed as random packing structures with irregular particles. The presented framework demonstrates a computational design following general programming logic as pre-processing, core computation and post-processing. The pre-processing module adopted 3D random packing with our previously captured rocks database. The core computation module adopted an extraction of the numerical scheme of LBM and a modification for heat conduction. The post-processing module introduced several programs, including temperature tracking, energy tracking, round-trip efficiency and heat flux distribution. The feasibility of expanding the lattice-based computation towards an up-scaled domain was discussed with digital tests mixed with realistic input. State-of-the-art techniques were presented to make the design of packed beds feasible for practical thermal analysis.

2.0 Methodology

2.1 The Framework

The general framework of the computation is demonstrated in Fig.1. The static structures of the packed bed were reconstructed with our validated packing algorithm [43]. The particle input process was improved by our irregularly shaped particle database [44]. The packing structure after construction was transformed into a virtual heat exchange device after the pre-processing. The core computation applied an

algorithm mathematically extracted from the logic of the D3Q7 LBM. The D3Q7 configuration was chosen for its straightforward physical correspondences of flux directions. The raw data from the lattice simulation then undergoes the post-processing steps, leading to the results in this study. In the aspect of multiscale modelling, the final result is an upscaled reflection of the mesoscale behaviour of heat exchange in heterogeneous media. The computation in this study was performed by GNU Octave [68] through independent programming.

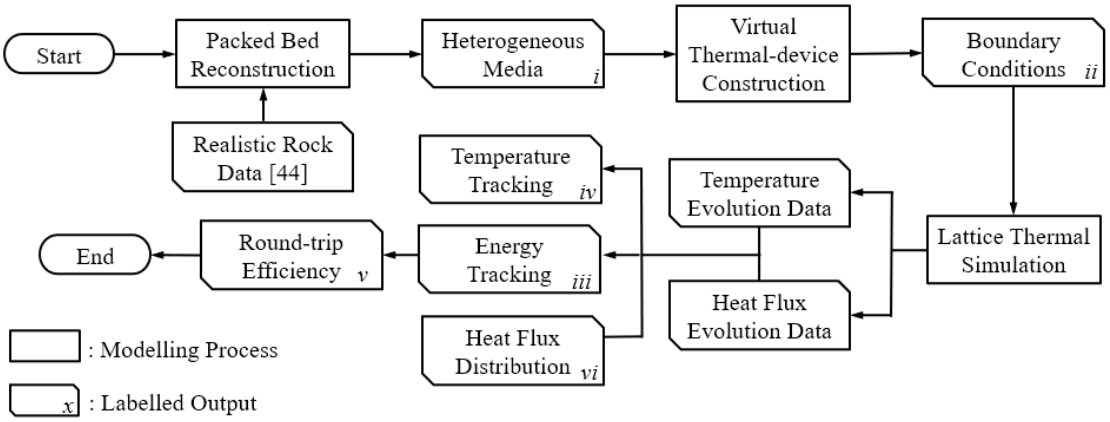

Fig. 1. The computational framework in this work

2.2 The irregular-shaped particle packing

The irregular-shaped particle packing algorithm is the same as our published version [43]. The reconstruction of the packed structure initially adopted an RSA placement of the irregular-shaped particles from the database. A downward movement was generally assigned to all the particles over the space, during which the contact of each particle triggered the horizontal movement. Mechanical interlock of one individual particle was activated when the resultant of motivating forces is less than the resultant of friction. As a result, the coefficient of friction served as the tuning parameter to realise varied packing configurations. Sampling was performed by extracting a sub-volume of the packed particles. Totally four digital samples were prepared for parameter control purposes. The solid phase fraction in this study is defined as the proportion of solid particle volume to the total volume. The fraction of connection is defined as the proportion of the volume of the connected solid phase to the volume of the solid within the total volume. The definition of the solid phase fraction and its conversion to the porosity is presented by Eq. 1.

$$\emptyset = \frac{V_s}{V} = 1 - p \tag{1}$$

where $\emptyset$ is the solid phase fraction; V_s is the volume of solid particles; V is the total volume, and p is the porosity. The differences in the solid phase fraction and fraction of connection for each sample are presented in Table 1.

Table 1 Basic Properties of the porous structures

	S1	S2	S3	S4
Solid Phase Fraction	53.05%	42.33%	34.93%	21.25%

Fraction of Connection	100%	100%	100%	99%

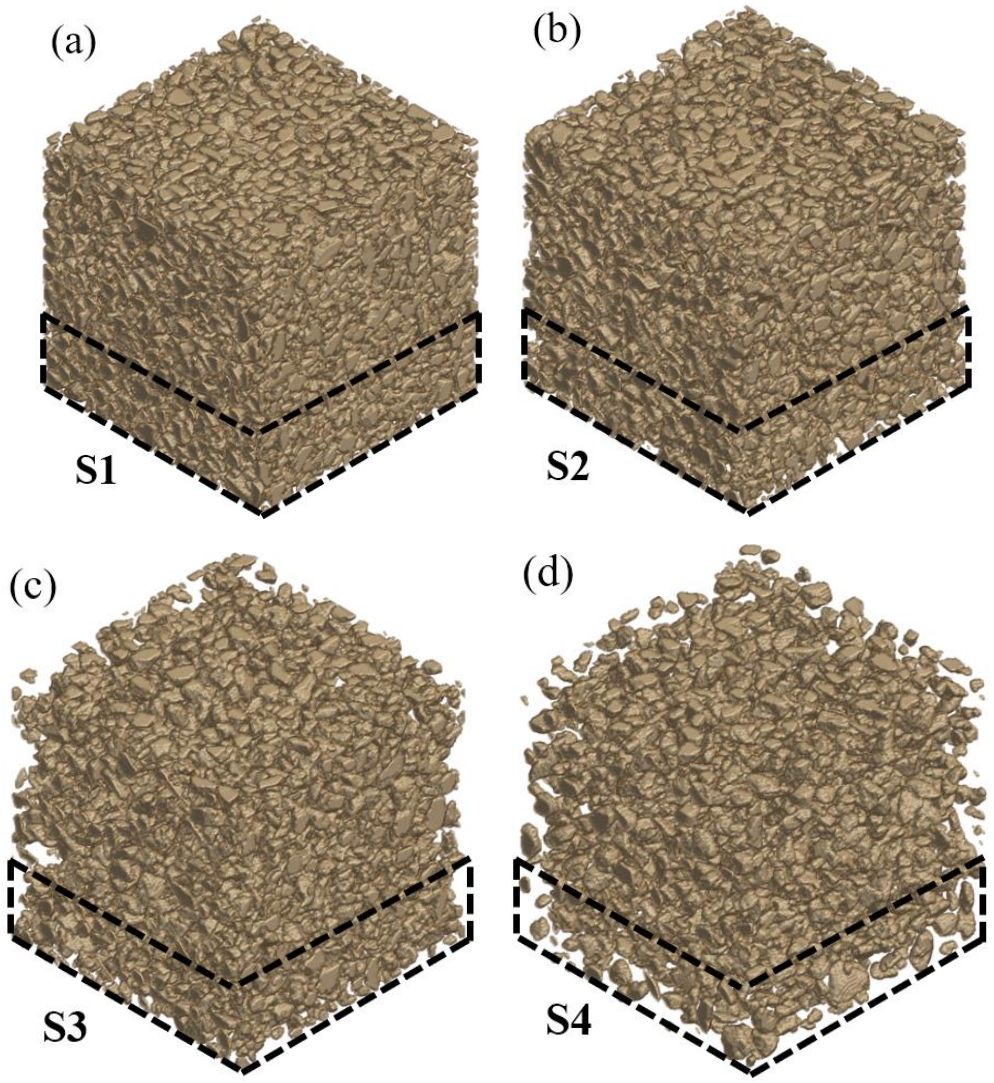

Fig. 2 Data *i*: Heterogeneous media with realistic particles. (a)The RCP media. (b)The first RLP media. (c) The second RLP media. (d) The RSA media

The packing structures with the above property listed in Table 1 are presented in Fig. 2, where the shaded zones are the sample extraction locations. The virtual device for heat conduction is demonstrated in Fig. 3, where the internal media adopts one of the samples extracted from the porous structures. The virtualism of this device is that the surrounding layer and bottom layer are completely thermal insulation, and the top layer is a materials-less conduction layer. The internal phase of the device is separated into the air phase and the solid phase. The air and solid phases adopted the thermal properties of air and sandstone, in which the values were defined by referencing the range of an open-source database [69] and previous studies [70,71]. The involved properties are thermal conductivity λ, mass density ρ, specific heat capacity C_p and volumetric heat capacity ρC_p. The specific heat capacity was manually scaled with 10^{-3} to accelerate the non-conduction simulation. The physical significance of this scallinng treatment is a deactivation of the particle scale reservoir when maintaining the geometrical propertis

and local conduction ability, which accelerate the thermal response of the same porous media in sample scale. Since the same treatment was simultaneously applied to all the sampels, the comprasion among sample with different packing structure can then be conducted more efficiently. The space scaling of the virtual device is 10^{-2}m per lattice unit length, and the above properties with length units were scaled accordingly during computation.

Table 2 Thermal properties of the phase in the virtual device

	λ ($\mathrm{Wm^{-1}K^{-1}}$)	ρ ($\mathrm{kgm^{-3}}$)	C_p($\mathrm{Jkg^{-1}K^{-1}}$)	ρC_p($\mathrm{Jm^{-3}K^{-1}}$)
Virtual Air	0.0250	1.205	1.004×10^3 (scaled)	1.210×10^3
Virtual Rock	6.500	2.700×10^3	0.963×10^3 (scaled)	2.600×10^6

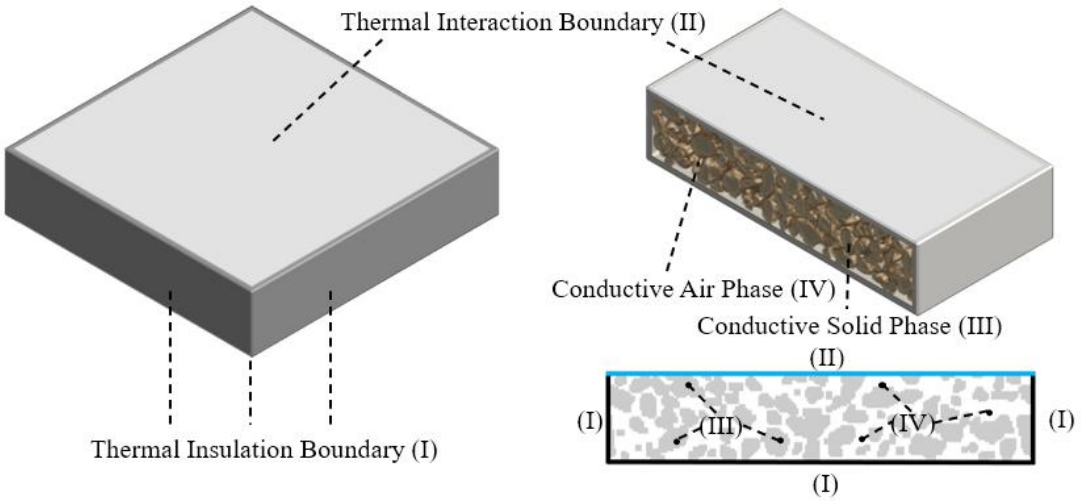

Fig. 3 Data *ii*: One virtual device for heat conduction in a porous medium

2.3 The lattice computation of heat conduction

The governing equation for the local heat flux driven by conduction is presented by Eq. 2, which is fundamentally a tensor form of Fourier's law.

$$\boldsymbol{q_{a,i}}(\boldsymbol{x}, t+\delta t) = \omega_i A \boldsymbol{K}(\boldsymbol{x}) \cdot \frac{\boldsymbol{T}(\boldsymbol{x}+\boldsymbol{e_i}) - \boldsymbol{T}(\boldsymbol{x})}{||\boldsymbol{e_i}||_2} \tag{2}$$

where $\boldsymbol{q_a}$ is a 4th order active heat flux tensor with seven directions; $\boldsymbol{x}$ is the cartesian coordinates vector; t is the computational time; δt is the unit time; ω_i is the directional weight factor scalar in the ith direction; A is the surface area scalar; K is the 3rd order conductivity tensor; $\boldsymbol{T}$ is a 3rd order temperature tenor; $\boldsymbol{e_i}$ is a directional unit vector in the ith direction of the seven directions and $||\quad||_2$ is the L2 norm. Consequently, the space scaling between the simulation and reality can be expressed as $||\boldsymbol{e_i}||_2 = 10^{-2}$m. The weight factor array containing the value of each ω_i is presented by Eq. 3, and the directional unit tensor containing $\boldsymbol{e_i}$ is presented by Eq. 4. The function of $\boldsymbol{\omega}$ is the control of the numerical computation speed and the anisotropic weight of the heat transfer in different directions.

$$\boldsymbol{\omega} = [\tfrac{162}{168}\ \tfrac{1}{168}\ \tfrac{1}{168}\ \tfrac{1}{168}\ \tfrac{1}{168}\ \tfrac{1}{168}\ \tfrac{1}{168}] \tag{3}$$

$$\boldsymbol{e} = \begin{bmatrix} 0 & 1 & -1 & 0 & 0 & 0 & 0 \\ 0 & 0 & 0 & 1 & -1 & 0 & 0 \\ 0 & 0 & 0 & 0 & 0 & 1 & -1 \end{bmatrix} \tag{4}$$

The principle of the algorithm is presented in Fig. 4. It is assumed that heat conduction occurs simultaneously on each surface of the space unit, which is a cube with a length of $||\boldsymbol{e_i}||_2$. The surface heat flux is decomposed into three orthogonal directions. By summing all the surface heat flux in the same direction, the body heat flux is therefore formed as presented in Fig. 4. The seven directions of a space unit include six surface normal vector directions and one zero vector from the centre. The above configuration guarantees the heat transfer from one space unit to its surrounding units while maintaining energy conservation. Long-range heat transfer is therefore modelled by an increment of computational iteration, which is presented in Fig.5.

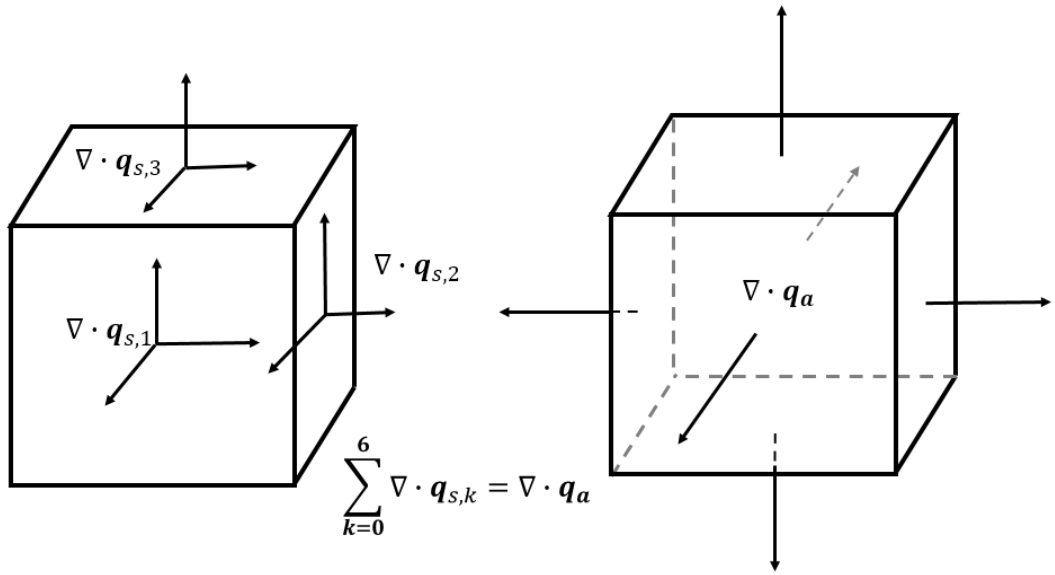

Fig. 4 The local principle of the lattice-based thermal conduction computation

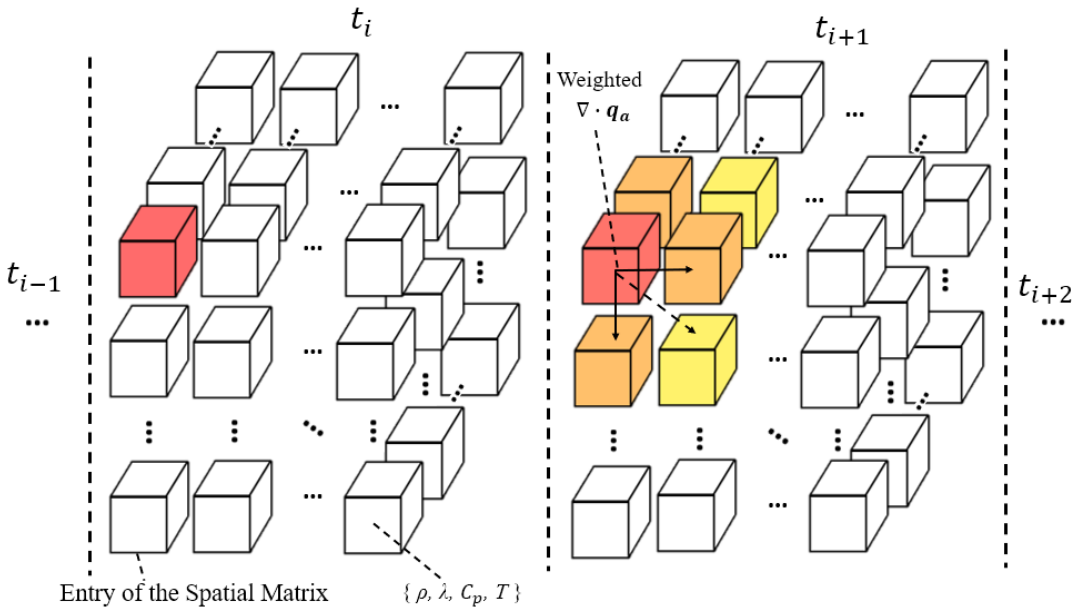

Fig. 5 The global principle of the lattice-based thermal conduction computation

The temperature change in each space unit is calculated with Eq. 5, which adopts the definition of specific heat capacity in the tensor form.

$$\Delta T(\boldsymbol{x}, t+\delta t) = \frac{\sum_{i=1}^{6} ||\boldsymbol{q_{p,i}}(\boldsymbol{x}, t+\delta t)||_2}{V\rho C_p} \quad (5)$$

where ΔT is the temperature change; $\boldsymbol{q_{p,i}}$ is the passive heat transfer into the space unit from its surrounding units, where $\boldsymbol{q_{p,i}}(\boldsymbol{x}, t+\delta t) = -\boldsymbol{q_{a,i}}(\boldsymbol{x}+\boldsymbol{e_i}, t+\delta t)$; V is the volume of the space unit with a value of $||\boldsymbol{e_i}||_2{}^3$; ρ is the mass density of the phase in the space unit and C_p is the corresponding specific heat capacity.

2.4 The digital tests

The effective conductivity test was conducted with four packed bed samples, in which the effective conductivity was defined with Eq. 6. The temperature gradient was defined as a constant gradient in the *k*th direction of the samples with 293.15K and 253.15 K on two opposite surface layers, respectively. The effective conductivity was measured in each cross-sectional layer of the internally packed structure with a thickness of one lattice unit length.

$$\lambda_{eff} = \frac{|\sum \boldsymbol{q_{a,k,A}}|}{\delta t A \omega_k} \frac{d}{\Delta T_k} \quad (6)$$

where A is the total area of the cross-sectional measurement; d is the thickness of the measurement area with unit lattice length; $\boldsymbol{q_{a,k,A}}$ is the active heat flux vector normal to the measurement cross-section towards the *k*th direction; ω_k is the *k*th weight factor in Eq. 3 and ΔT_k is the temperature difference between the nearest lattices in the *k*th direction. In this study, *k* took the value of 7.

Two groups of digital experiments were developed to test the energy performance of the porous media. The first group of experiments, which was denoted as the R group, defined the internal grains of the virtual device as the heat source. The second group of experiments, which was denoted as the S group, defined the thermal interaction boundary of the virtual device as a constant temperature heat source. The details of the digital experiments configuration are further presented in Table 3.

Table 3 Thermal properties of the phase in the virtual device

R Group	Top Layer	Grains	Pores	Insulation Layers
Initial Temperature	253.15K	293.15K	273.15K	250K
Boundary Condition	Constant Temperature	Full Conduction	Full Conduction	Full Bounce-back
S Group	…	…	…	…
Initial Temperature	293.15K	253.15K	253.15K	250K
Boundary Condition	Constant Temperature	Full Conduction	Full Conduction	Full Bounce-back

Six digital tests were conducted in each group of experiments. The heat exchange

measurement was performed by measuring the heat intake and escape from the heterogeneous media during temperature change per unit of time. Total energy exchange was performed by the accumulation of the heat exchange rate data over time. Mean temperature tracking was performed by calculating the average temperature of the solid phase and pore phase within the virtual device in each computational iteration. Round-trip efficiency in this study is defined as the ratio of the same thermal characterisation in the S group and the R group. Consequently, the heat round-trip efficiency was calculated as the ratio of heat exchange rate data in the heat exchange rate tests, as presented by Eq. 7. The energy round-trip efficiency was calculated as the ratio of total energy exchange values in the total energy exchange tests, as presented by Eq. 8.

$$\eta_q(t) = \left|\frac{Q_S(t)}{Q_R(t)}\right| = \left|\frac{\sum_x \sum_{i=1}^{6} \boldsymbol{q_{S,p,i}}(\boldsymbol{x},t)}{\sum_x \sum_{i=1}^{6} \boldsymbol{q_{R,p,i}}(\boldsymbol{x},t)}\right| \quad (7)$$

$$\eta_E(t) = \left|\frac{E_S(t)}{E_R(t)}\right| = \left|\frac{\sum_t Q_S(t)}{\sum_t Q_R(t)}\right| \quad (8)$$

where $\eta_q(t)$ is the heat round-trip efficiency at time *t;* $Q_S(t)$ is the heat exchange amount over the whole volume in the S group at time *t*; $Q_S(t)$ is the heat exchange amount over the whole volume in the R group at time *t;* $E_S(t)$ is the accumulated energy in the S group at time *t,* and $E_R(t)$ is the accumulated energy in the R group at time *t*. Passive local heat was adopted during the computation since it is the driving factor for temperature change, as shown in Eq. 5.

The dimensionless feature of the round-trip efficiency eventually cancelled the influence from specific heat capacity scaling, which was simultaneously applied to the S group as the numerator and the R group as the denominator. The above tests performed characterisation of the heat transfer behaviour of the virtual device from an integral perspective. In terms of local heat transfer, multiscale heat flux distribution tests were performed to record the heat flux in each space unit of the porous media. Heat flux was defined as the amount of heat passing through a unit area per lattice unit time, and a degree of magnitude of 10^{-2} $\mathrm{J/m^2ls}$ was defined as the demarcation line between microscopic flux and macroscopic flux in this study.

3.0 Results and Discussion

3.1 Analytical and experimental validation

The visualised results of the temperature distribution as a result of the heat conduction are presented in Fig.6. In comparison with the previously mentioned models, the simulation in the study demonstrates a strong capability to model the heat transfer in porous media with extreme complexity. Fig. 6(a) presents the simulated heat transfer phenomenon and the resulting temperature distribution over the irregular pathway in the virtual device. It can be noticed that the full bounce-back condition of the insulation boundary successfully functions as the thermal inert wall for the heat transfer process. The constant temperature condition of the interaction boundary functions well for the media-environment interaction, near which the irregularly distributed temperature drops as a practical expectation. Fig.6(b) presents the cross-section temperature contour. It can be noticed that the connected pores perform an essential path for the heat release

from the particles, and the early-age heat flux can be calculated with the temperature gradient based on a realistic potential field.

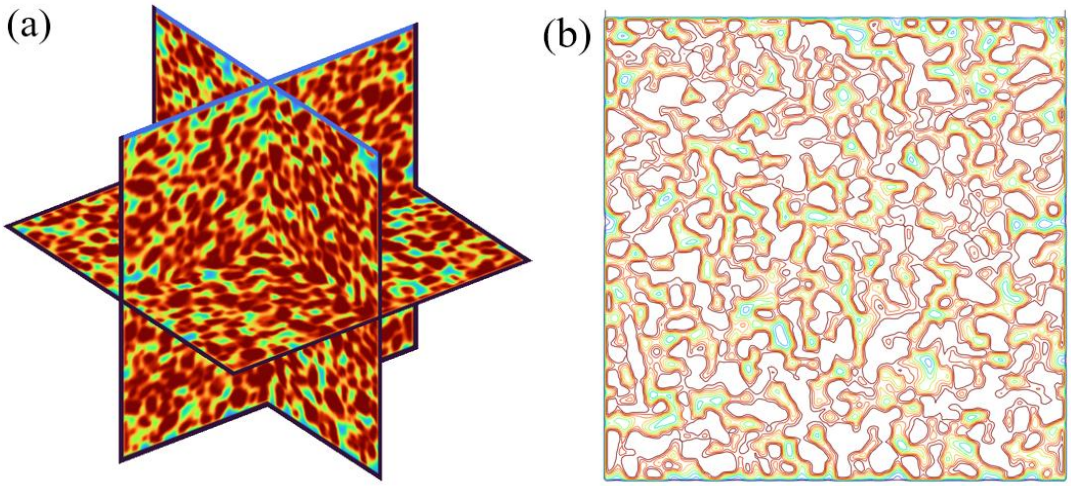

Fig.6 Visualised temperature result within RCP media. (a) Temperature 3D spatial distribution. (b) Temperature 2D crossectional contour.

Theoretical validation was performed with shell heat conduction with simple geometry. A one-dimensional temperature variation of $T = 2\sin(x) + 273.1$ was adopted for the scaled analytical calculation. The analytical solution can be treated as one of the top-down solvers since it is a solution of the partial differential equation with a globally homogeneous assumption. In this comparison, the unit length of the analytical solution was scaled from m to cm for the later acceleration of the numerical simulation. On the other hand, the solution in this study is one of the bottom-up solvers since the solving process treats the global geometry with heterogeneity. Fig.7 demonstrates the comparison between the scaled analytical solution and the solution from this study. The comparison provides a strong agreement between the scaled analytical solution and the solution in this work in the internal volume of the cubic shell. This validation provides theoretical support to adopt the simulation scheme in heat transfer analysis with complex geometry. Hence, the routine in this work presents a feasible solution to analyse heat transfer behaviour.

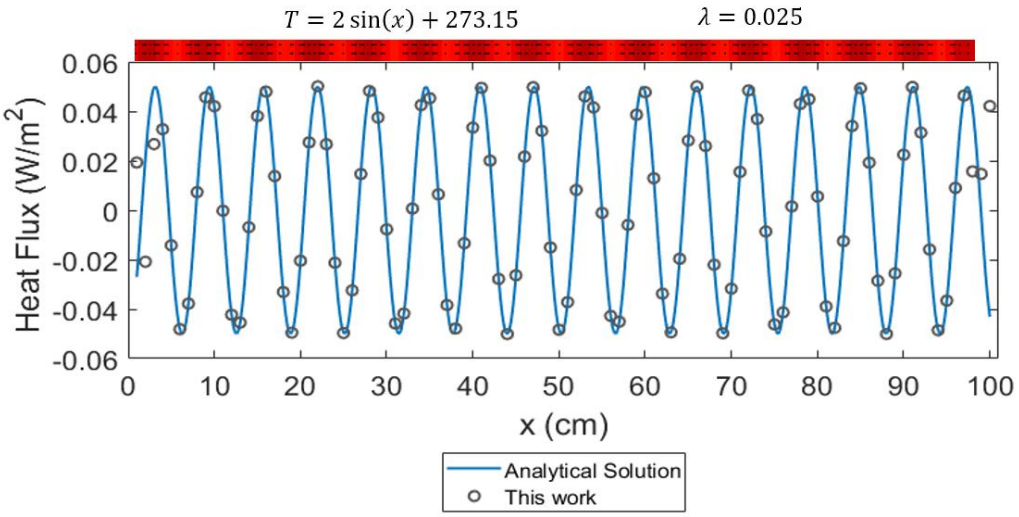

Fig.7 Comparison between the scaled analytical solution and numerical solution in this work

Experimental validation was performed with the well-presented effective conductivity measurement from [72,73], in which the research subject shared a similar feature of packed beds with non-metallic material to this work. The difficulty of analysing the thermal behaviour of packed structures is its stochasticity, which leads to a variation of effective conductivity both in 2D and 3D. Such stochasticity was reflected in the cross-sectional difference in the same sample. Fig. 8 presents the cross-sectional measurement of the effective conductivity of the four samples in the digital conduction system. It can be noticed that the effective conductivity is positively correlated with the solid phase fraction. In previous studies of a similar conduction system in reality, an effective conductivity range of 1.25 to 3.96 W/mk was experimentally observed in packed beds with quartz-rich rocks [72]. This range is in accordance with the digital observation range in S1, S2 and S3 samples. The major difference between S1-S3 and S4 samples is the reaching of 100% solid phase connection, and the unreached full connection made the S4 sample unrealistic in a non-flotation environment. As a further comparison, another experimental observation of the effective conductivity in packed beds with iron-manganese oxide demonstrates a range of 0.1 to 1.8 W/mk [73]. Although this range covers the S4 range well, it is argued that such accordance is a combined result of different packing structures and material-level conductivity. The above validation indicates that the computation framework proposed in this study digitally recovers the heat conduction system of packed rock beds, and packed beds with other materials can also be modelled with the framework to some extent.

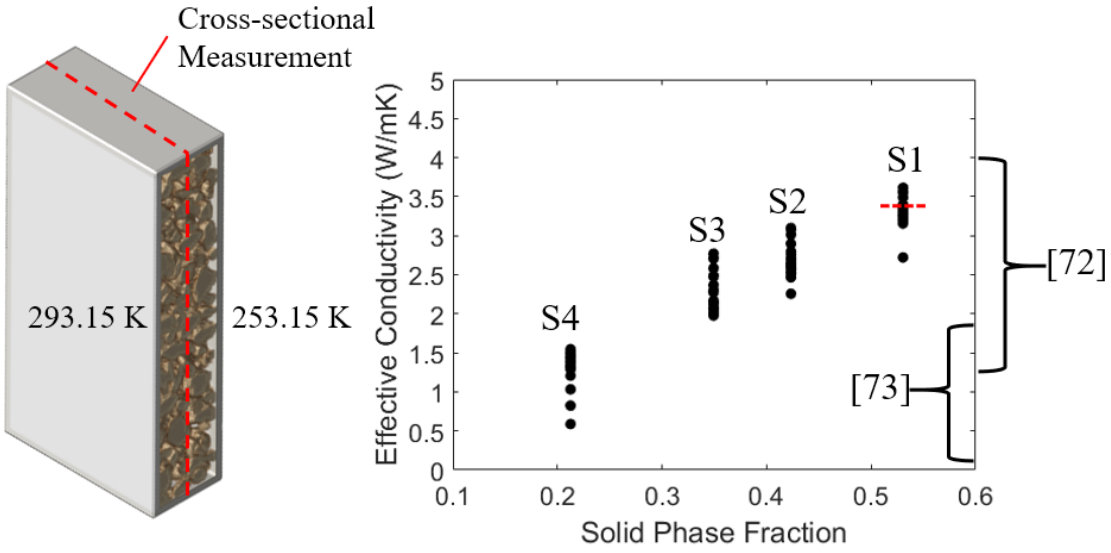

Fig. 8 Comparison between the effective conductivity from this work and previous experimental measurements from [72,73]

The above results show that the scaling treatment of the specific heat capacity did not alter the heat conduction performance under that pre-defined thermal load. The presented framework is fundamentally a tensor computation of Fourier's law in multidirection, which does not have the involvement of the heat capacity. Hence, the scaling of the specific heat capacity does not influence the heat conduction behaviour during each time step. The following sections demonstrate the bottom-up thermal and energy analysis enabled by this validated conduction foundation.

3.2 The heat and energy tracking

The time-dependent heat exchange is demonstrated in Fig. 9. The measurement was conducted in the internal space of the virtual device, hence it is a bulk measurement of the heat conduction result from the heterogeneous media. Fig. 9(a) presents the energy loss rate from the virtual device. It can be noticed that all the samples shared a similar pattern of the released heat rate development. The released heat is rapid in the early age, which is about 1×10^5 lattice seconds. Considering the time scaling, it can be found that the natural release of the stored energy in all the samples can function as the heat source for 12 lattice hours, which corresponds to 43200 lattice seconds. In other words, the virtual device with a random packing configuration is capable of providing heating in the day and night cycles. The upper limit of such heat-providing function is located at 2×10^5 lattice seconds, which is 55.6 lattice hours. As a result of the above measurement, the application of porous rocks considering other heat transfer types will reduce this upper time limit. The balance of heat release amount as the heating duration for ordinary application to replace traditional air conditioners shall be designed with an upper time limit covering the desirable heating duration. In terms of the influence of solid phase fraction on the magnitude of released heat, there is a clear pattern that the absolute value of the heat around the time limit follows a decreasing sequence of S1R, S3R, S2R, and S4R. Consequently, it is deduced that the increment of the solid phase fraction can generally increase the released heat. Although such an increment in the realised energy rate is in favour of infrastructure heating, the solid phase fraction cannot be increased to 100%. One reason is that there needs to be an air percolation path to enable effective airflow convection. The other reason is that there exists an upper limit for the solid phase fraction for the packing of arbitrarily shaped rocks, which is similar to the RCP limit for spherical particles. Fig. 9(b) presents the stored heat of all the samples in the S group. The stored heat development also follows a pattern of rapid heat exchange at the early stage and slow heat exchange at the late stage. There also exists a time limit of 1×10^5 lattice seconds for the conversion of fast energy storage and slow energy storage. Consequently, the natural heat conduction in a packed bed with a random packing configuration is capable of providing balance to the day and night cycles. This similar pattern with the energy release rate indicates that a proper design for the energy storage process can also be beneficial to the energy release process. The heat storage design for practical usage of packed beds shall also consider the time limit to make full use of the energy properties. The influence of solid phase fractions on the magnitude of stored energy also follows a clear pattern, in that the increment of the solid phase fraction enhanced the amount of the stored energy, as demonstrated by the sequence of S1S, S3S, S2S, and S4S. The above result indicates that the heat storage and release of the porous media in the virtual device share the same logic when it comes to the correlation between solid phase fractions and absolute values of heat exchange. Caution shall be awarded to adopt a particle size distribution of rocks leading to sufficient airflow path percolation, which is above 10% porosity [74]. According to the highest solid phase fraction of 53.05% reached in this study, the higher solid phase fraction of 64% in RCP with spherical particles arguably indicates a more desirable basic unit choice. However, the practical material choice for a packed bed cannot guarantee the perfect roundness of each basic particle. Hence, arbitrarily shaped particles, as demonstrated in this work, are necessary for the design and application in reality. One

critical time section for both energy release and storage is 1×10^5 lattice seconds or 27.78 lattice hours for serviceability.

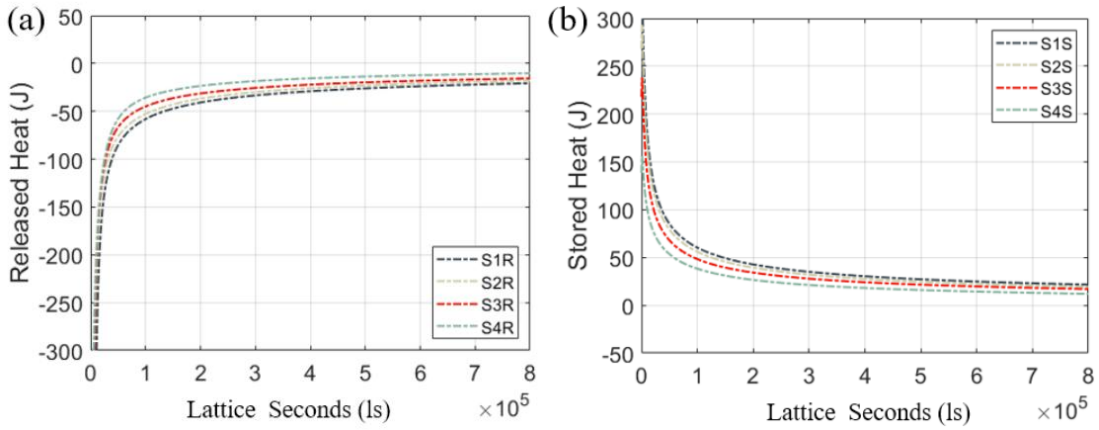

Fig.9 (a) Heat tracking in the R group. (b) Heat tracking in the S group.

In an attempt to extract the correlation between time and heat exchange for general engineering usage, regression analysis was further performed with the data from heat tracking. The principle of the function choosing is that the curve should fit the form of data development well, with a relatively low coefficient of determination (R^2). After a thorough comparison of the commonly used functions, it was found that the exponential function, as demonstrated by Eq. 9, could properly describe the linear correlation for heat release and storage development versus time. The coefficients are listed in Table 4.

$$\sum q = c_1 e^{c_2 x} + c_3 e^{c_4 x} \tag{9}$$

Table 4 Coefficients of the heat regression analysis

R Group	S1	S2	S3	S4
c_1	-2.2563×10^4	-4.1945×10^3	-3.3921×10^3	-1.9068×10^3
c_2	-0.0019	-0.0010	-0.0011	-0.0011
c_3	-2.8482×10^3	-133.5942	-241.6851	-267.4368
c_4	-2.1703×10^{-4}	-5.3568×10^{-6}	-1.9056×10^{-5}	-2.7500×10^{-5}
R^2	99.77%	97.17%	96.61%	95.74%
S Group	…	…	…	…
c_1	233.6320	204.4260	162.5371	100.2107

c_2	-5.2438×10^{-5}	-4.9219×10^{-5}	-4.6113×10^{-5}	-3.5980×10^{-5}
c_3	63.0685	58.1583	49.4047	37.9333
c_4	-1.5842×10^{-6}	-1.6222×10^{-6}	-1.5576×10^{-6}	-1.6363×10^{-6}
R^2	97.99%	98.10%	98.16%	98.60%

The above heat exchange was defined as the energy difference of the porous media during temperature changes between sequential interactions. Hence, the energy development of the same media can be calculated by discrete integration. Fig. 10 presents the energy tracking results in a complete sense. It can be noticed that the influence of the solid phase fraction is more clearly demonstrated than the heat exchange during local iteration. Fig. 10(a) presents the released energy in the R group as the energy reduction of the internal structure of the virtual device. It can be noticed that the energy amount followed an increasing order of S1R, S3R, S2R and S4R. This pattern again demonstrates the general trend that the solid phase fraction increment raises the energy release amount. The previous threshold for heat release drop is reflected by the stable gradient of total energy development, which demonstrates the stability of the developed algorithm for a long duration. Fig. 10(b) presents the stored energy in the S group. The energy amount at the same time also followed the increasing order of S1S, S3S, S2S and S4S. This similarity shows that the solid phase fraction in the random rock packing affects energy release and storage in common. The threshold for heat storage drop is again reflected by the stable gradient of the total energy storage. The above behaviour of stable energy gradient concludes that the representative samples are sufficient to provide energy exchange for day and night cycles for ordinary applications. The most important finding of the disordered energy magnitude order between S2R/S and S2R/S. This irregular energy development indicates that there exists a balanced line between 34.93% and 42.33% solid phase fraction. The scientific significance of finding this balanced line is that it is the critical solid phase fraction where the short-range particle-air heat exchange and medium-range particle-particle heat transfer offset each other.

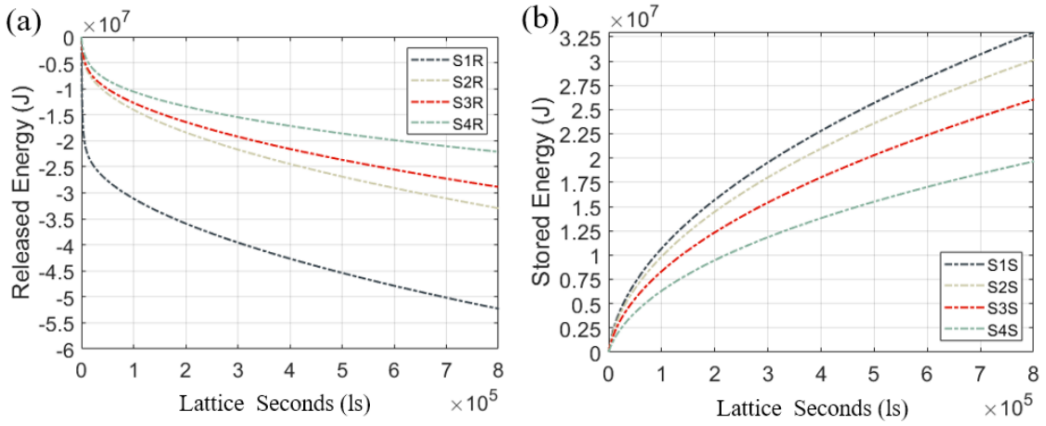

Fig.10 Data *iii*: (a) Energy tracking in the R group. (b) Energy tracking in the S group.

Regression was again performed for general engineering usage. It was found that the power function, as demonstrated by Eq. 10, can properly describe the numerical behaviour between the energy and time correlation. The coefficients are listed in Table 5. It is interesting to notice that the coefficients of determination with the kept number of digits have reached a high value. This high value demonstrates that the physics of the bottom-up computation is relatively complete. The strength of physics-based simulation is that individual influences can be studied separately, and what was focused on in this part of the work is the influence of short-range particle-air heat exchange and medium-range particle-particle heat transfer. The above results show that the power function with the coefficients could serve as the evolution equation form for energy development in the emphasised scenario.

$$E = c_1 t^{c_2} + c_3 \tag{10}$$

Table 5 Coefficients of the energy regression analysis

R Group	S1	S2	S3	S4
c_1	-1.8543×10^4	-6.0235×10^4	-6.0882×10^4	-1.7622×10^4
c_2	0.3913	0.4588	0.4477	0.3556
c_3	-1.4095×10^7	-2.1152×10^6	-2.0433×10^6	1.1226×10^5
R^2	99.41%	99.96%	99.95%	99.97%
S Group	…	…	…	…
c_1	3.2501×10^4	3.5172×10^4	2.6658×10^4	3.0838×10^4
c_2	0.5115	0.4998	0.5094	0.4802
c_3	-1.0424×10^6	-1.2212×10^6	-1.0360×10^6	-1.3625×10^6
R^2	100.00%	100.00%	100.00%	99.98%

Although the above results present a statistically well-fitted regression of the heat and energy evolution, the physical correspondence of the coefficients is still open to discussion. From the current observation in this study, the c_1 and c_3 coefficients in Eq. 9 of the S group appear to be more strongly correlated with the solid phase fraction or air fraction. Considering that packed beds in a simple form can be treated as a composite with solid phase and pores, Eq. 9 of the S group demonstrates a higher generalising value for its dual-component formate. However, it needs to be mentioned that identification of the constitutive equation still requires a profound investigation, both mathematically and experimentally.

3.3 The Temperature and Efficiency Tracking

The internal temperature of the virtual device was measured as the average temperature over all the space units of the porous media. Fig. 11 demonstrates the temperature tracking results over the full time. The general expectation that the R group shall have a temperature drop and the S group shall have a temperature rise is successfully fulfilled. Fig. 11 (a) presents the temperature development of all the samples in the R group. It can be noticed that the average temperature follows a decreasing order as S1R, S2R, S3R and S4R. This comparison indicates that the solid phase fraction is positively correlated with the average temperature magnitude. One noticeable result is that the average temperature in the S1 sample is much higher than the rest, although the solid phase fraction of S1 is only about 10% higher than that of S2. The digital preparation of the S1 sample adopted a coefficient of friction of 0, which led to the RCP configuration with irregular-shaped particles. This result directly points out that RCP is in favour of the temperature maintenance of packed beds. Fig. 11(b) presents the temperature development of all the samples in the S group. The total temperature increment for each sample follows an increasing magnitude order of S1S, S2S, S3S and S4S. This result shows that the packed bed with a higher solid phase is less sensitive to heating or cooling. The proportional gap between the temperature of S1 and S2 again confirms the temperature-maintaining ability of the RCP configuration. The increase in solid phase fraction formed a solid pathway with decreased distortion. On the other hand, the corresponding decrease in air fraction caused an increased distortion of the connected pore space. This increase in the distortion further increases the internal pathway of the air phase with low conductivity, which tends to destabilise the spatial temperature profile within the overall stabilisation trend through the uniformity of material distribution. Considering the name of the packed bed, such a finding indicates that this thermal device may function well as a literal bed in the cold regions. In this scenario, the RCP configuration in this study already provides an improvement to the design of a type of traditional bed in northeastern Asia. The direct suggestion is that filling the originally empty chamber of this type of bed exist in the suburban area with closely packed rocks can help to maintain the temperature during low-temperature nights. The conceptual diagrams of the existing thermal application and an enhanced re-design with randomly closed-packed beds are presented in Fig. 11(c) and Fig. 11(d), respectively.

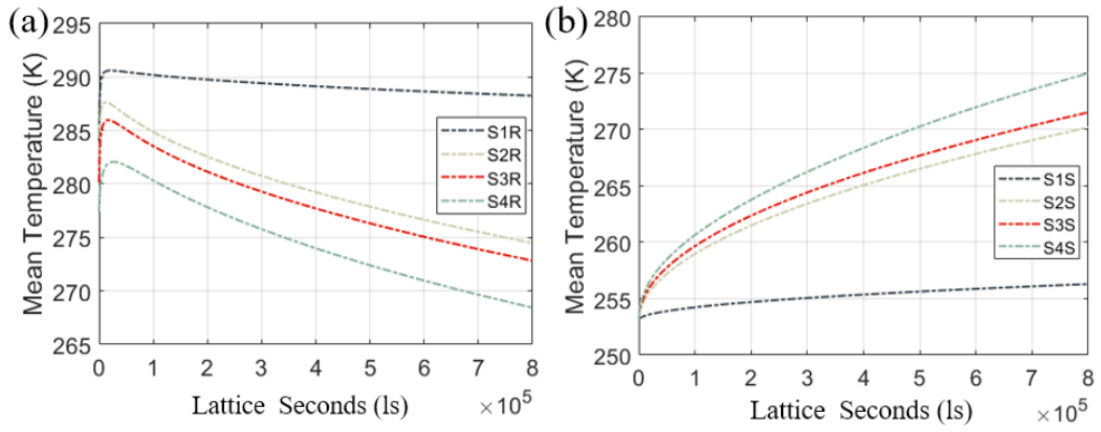

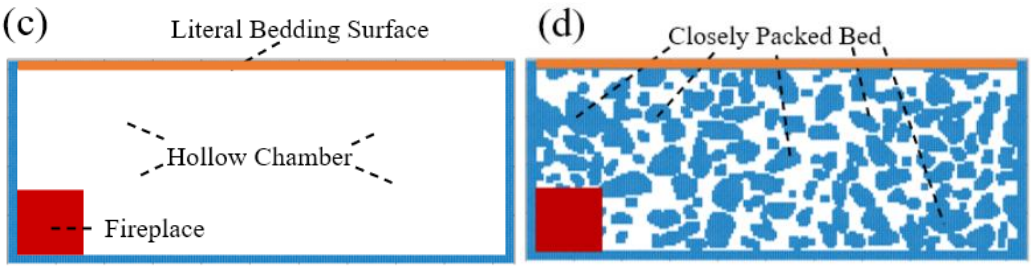

Fig.11 (a) Data *iv*: Mean temperature tracking in the R group. (b) Data *iv*: Mean temperature tracking in the S group. (c) An existing thermal device for domestic heating. (d) An improvement in the thermal device is suggested by the results.

The round-trip efficiency is a characterisation of the energy storage and release performance in a thermal device. Fig. 12 demonstrates the round-trip efficiency of the virtual device in this study. The general trend of the recorded round-trip efficiency shows an increasing early development until a relatively stable development is reached. Fig. 12(a) demonstrates the heat round-trip efficiency of all the samples. The figure demonstrates that 100% efficiency was reached within a time threshold of 1×10^5 lattice seconds, which corresponds to the shift from fast energy exchange and slow energy exchange in the previous discussion. The stable heat round-trip efficiency shows an increasing magnitude order following S1S/R, S2S/R, S3S/R, and S4S/R, and the highest value of all the samples is below 120%. It needs to be noted that the disordered S2 and S3 sequences from the heat tracking no longer exist. Hence, a pattern that the decrease of the solid phase fraction enhances the heat intake efficiency can be concluded. In other words, an increment of the solid phase fraction enhances the heat output efficiency. Fig. 12(b) presents the energy round-trip efficiency of all the samples. Although the heat round-trip efficiency in local time can reach a value of more than 100% in the later stage, the heat round-trip efficiency was always within 100%. This behaviour satisfies the expectation that there always exists energy loss during the energy storage and release cycles. In this study, the major energy exchange has already occurred during the early stage, indicating that the time threshold of 0.5×10^5 lattice seconds or 13.89 lattice hours is another critical time section for efficiency. Additional heat transfer, including convection and radiation, can further control this time threshold to fully cover the service duration.

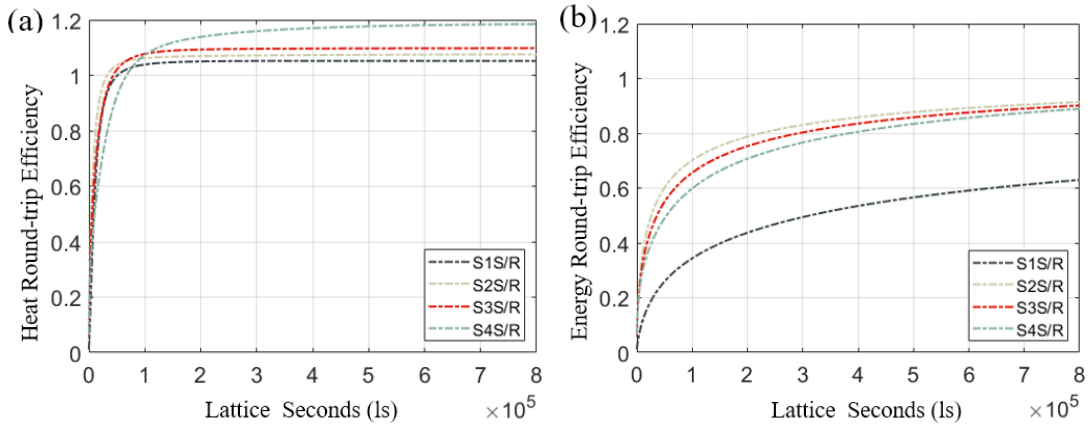

Fig. 12 Data *v*: (a)Heat round-trip efficiency. (b) Energy round-trip efficiency.

Returning to the settings of the digital experiments, it can be generally summarised that the decrease in solid phase fraction led to an increase in the round-trip efficiency. The

specific definition of round-trip efficiency in this study indicates that the heat intake behaviour in the sample with a lower solid phase fraction is more effective than that in the sample with a higher solid phase fraction. The heat conduction routine in packed beds inevitably has local pathways of solid-solid, solid-air and air-air. The decrease in solid phase fraction reduced the proportion of solid-solid routine while maintaining the global solid phase connection because of the percolation. From the perspective of the heat intake, there exists a global pathway with high conductivity from the thermal interaction boundary to its opposite end. As a result, the energy intake follows a dominating pathway of interaction boundary, solid skeleton, to the surrounding air phase. From the perspective of the heat release, the solid skeleton functions as roots surrounded by the air phase with energy. Although the solid phase skeleton is the same, the low conductivity of the surrounding air phase slowed down the internal energy escape of the packed bed. Although a pathway opposite to the energy intake exists during the energy release, it is less dominant since the slow heat conduction in the connected air phase is more influential when it is placed at the source position. The decrease in the solid phase fraction and the corresponding increase in air fraction enhance this effect, leading to a higher energy storage efficiency of the conduction-dominated packed bed.

3.4 Heat flux distribution in the critical time sections

The advantage of the bottom-up approach is its ability to provide local data in each space unit, which further enables the statistical analysis of the heat distribution. Fig. 13 presents the heat flux distribution in the R group with multiscale views, in which the flux was defined as the amount of heat through the lattice unit area (10^{-4} m^2) and lattice unit time. Three instantaneous time sections were sampled, including 0 lattice seconds, 0.5×10^5 lattice seconds and 10^5 lattice seconds. The sampled time sections have covered the previously found time threshold. Fig. 13(a) illustrates the heat flux distribution at the initial time section of the S1R test. It can be noticed that the distribution is a composite of two heat transfer behaviours, the major trigger of which is the internal particle-air interaction and the external boundary-environment interaction. The proportion of the microscopic heat flux was 54.58%, and the macroscopic heat flux was 45.42%, where the absolute value of the heat flux defines the observation scale instead of length. Although the values of the microscopic and macroscopic heat flux are distinguished, it was found that the generalised logistic function as presented in Eq. 11 can provide a fitting recovery of the discrete distribution.

$$f(x) = \frac{\gamma}{\sigma}\frac{\exp\left(\frac{\mu-x}{\sigma}\right)}{\left[1+\exp\left(\frac{\mu-x}{\sigma}\right)\right]^{\gamma+1}} \tag{11}$$

where μ controls the mean location, σ controls the scale, and γ controls the shape of the distribution. The composite distribution has a negative shift of μ, and the macroscopic distribution has a positive shift of μ. This indicates that the macroscopic heat flux corresponds to the particle-air interaction since the R group was dominated by heat release. On the other hand, the microscopic heat flux corresponds to the boundary-environment interaction.

Fig. 13(b) presents the heat flux distribution at the 0.5×10^5 time section of the S1R test. In comparison with the initial time section, the proportion of the microscopic

distribution was significantly increased. This behaviour shows that the boundary-environment interaction becomes the major cause of heat flux formation. The generalised logistic function can still represent the discrete distribution with certain numerical modifications. The distribution function for the microscopic distribution was found to only have reduced σ, which means the shape of the mid-time distribution curve becomes sharper than that of the initial distribution. This statistical behaviour indicates that the boundary-environment interaction has triggered decreased grading of the absolute values of the heat flux. On the other hand, the reduced σ value also appears in the macroscopic distribution, indicating a decreased grading in the particle-air interaction. This reduction of σ may also be caused by the increased grading of the microscopic heat flux as a result of the statistical conservation of the composite distribution. Fig. 13(c) further demonstrates the heat flux distribution at the 10^5 time section of the S1R test. The proportion of the microscopic heat flux was slightly increased following the same pattern of the changes from the initial time section to the 0.5×10^5 time section. In comparison with the 0.5×10^5 time section, the 10^5 time section led to the same distribution function. This behaviour demonstrates that the boundary-environment interaction becomes stable from 0.5×10^5 to 10^5 time sections. The trend of σ decreasing still appears in the macroscopic interaction, indicating that the heating potential of the packed bed was still not fully released. The microscopic mechanism of heat conduction mainly relies on the molecular energy exchange between two adjacent lattices. The heat conduction in packed beds is contributed by the vibration of molecular-level particles in the solid phase, the molecular free motion and collisions in the air phase, and the energy transfer at the interface. The interface temperature equilibrium is an important sign of reaching thermal stability. The initial condition of the high temperature difference at the interface of the R group caused the increased proportion of the heat flux with high magnitude. The interface then gradually reached temperature equilibrium, which simultaneously reduced the proportion of the heat flux with high magnitude.

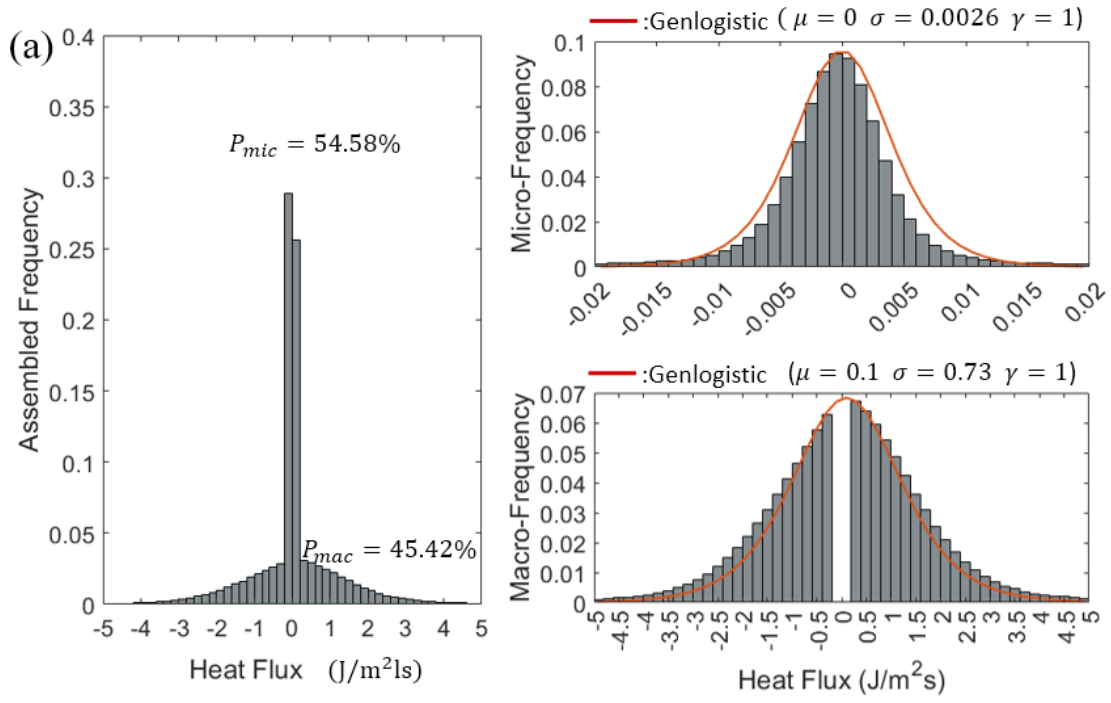

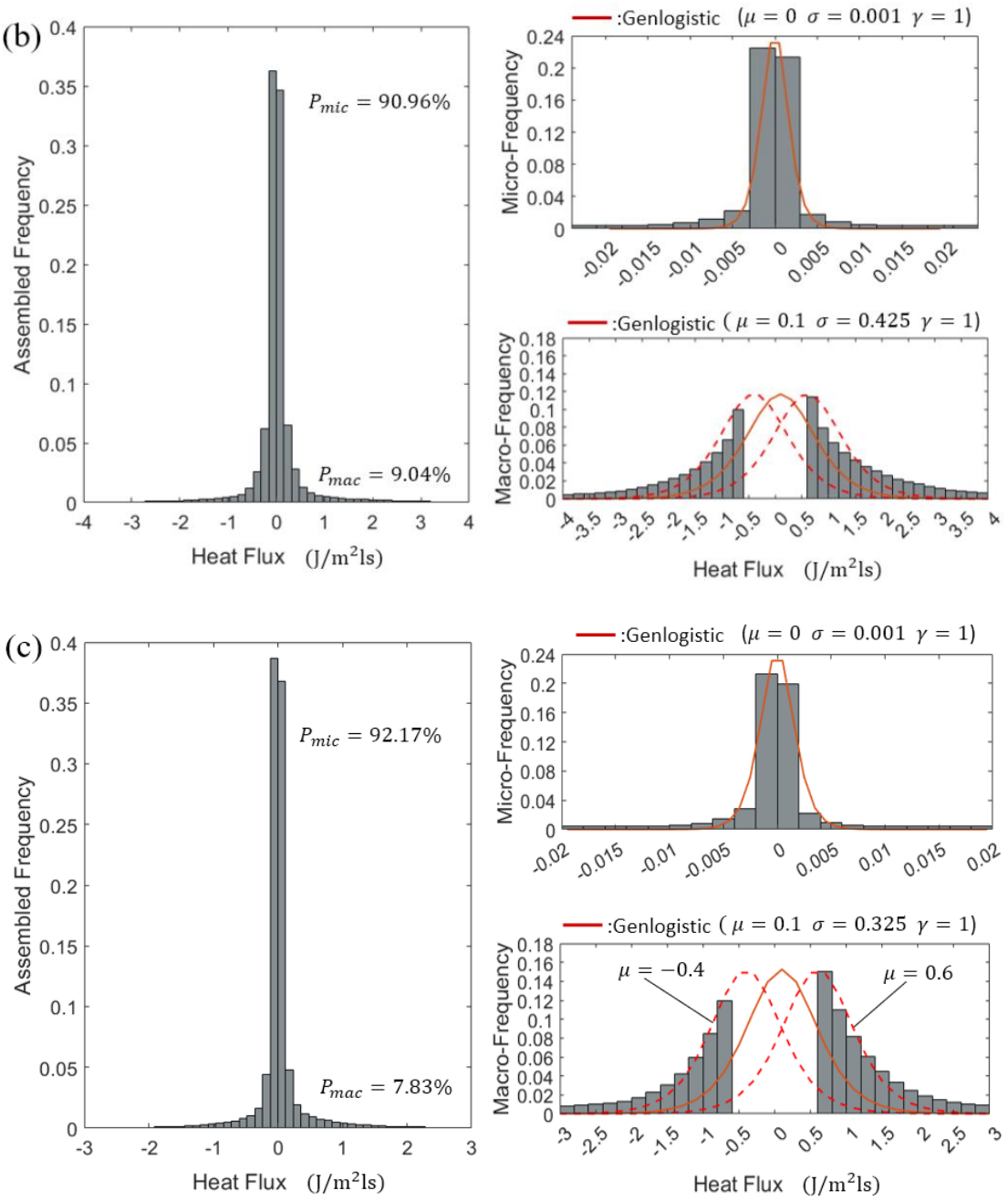

Fig.13 Data *vi* Heat flux distribution in R group at (a)0 ls, (b)0.5×10^5 ls and (c) 10^5 ls

Fig. 14 presents the heat flux distribution in the R group with multiscale views. Since R ground adopted simplified thermal conditions at the initial time section, the major heat flux generation occurred from the boundary-environment interaction. As a result, the microscopic heat flux distribution is dominant from the initial time section to the 10^5 time section. Fig. 14(a), (b) and (c) further present the heat flux distribution at 0, 0.5×10^5 and 10^5 time sections of the S1S test, respectively. A decrease in the absolute value grading can be noticed with an increment of time. This decrement indicates that the proportion of the boundary-environment interaction became less significant, although still dominating, through the recorded time section. Since the overall heat flux distribution is a composited distribution with heat flux generated from boundary-environment interaction and particle-air interaction, the decrement in the proportion of boundary-environment interaction will logically lead to an increment of the particle-air

interaction proportion. The major performance of a thermal device relies on its interaction with the external environment during energy storage. The initial condition of the S group did not have any internal temperature difference. The sample scale temperature difference triggered the heat conduction for the solid phase, the air phase and the interface. Because of the difference in heat conduction pattern, local temperature differences were formed in directions not parallel to the global temperature difference. Such local temperature differences accumulated during the time points of the measurement, resulting in a gradually increased proportion of heat flux with high magnitude. The significant contribution of the boundary-environment interaction to the heat flux generation was also reflected by the development of the round-trip efficiency in Fig.12. When it comes to storage efficiency, the packed bed would seek an enhancement for local particle-air interaction through heat transfer other than conduction.

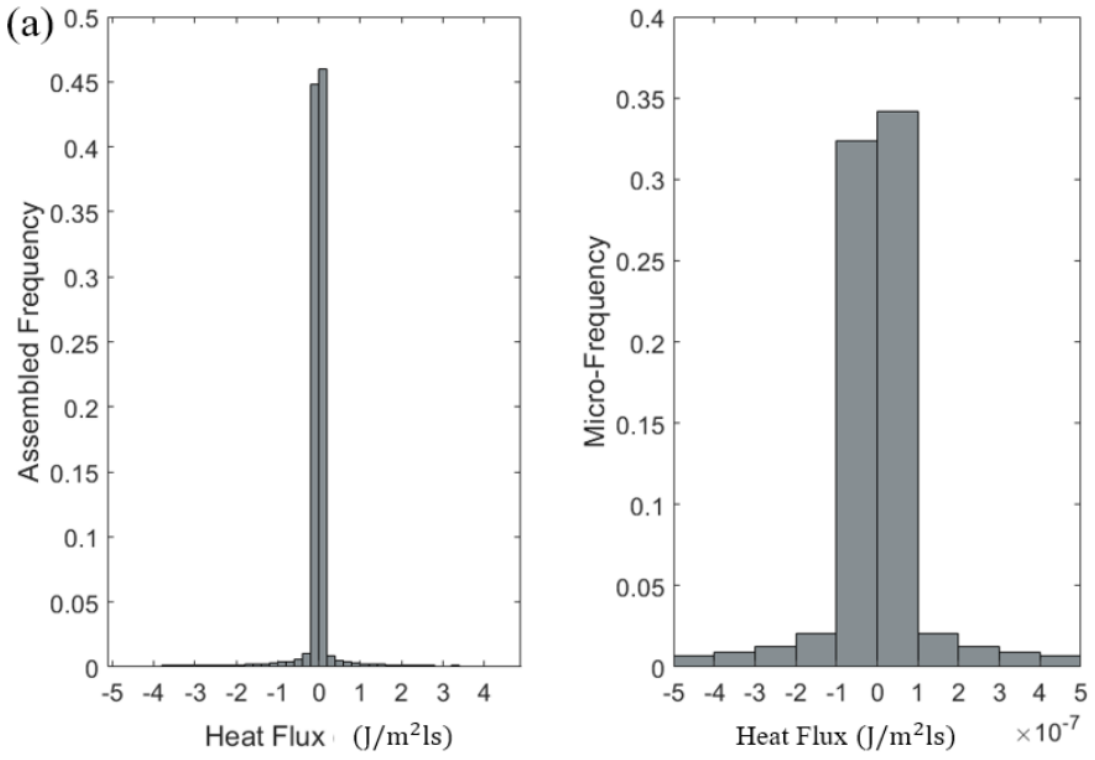

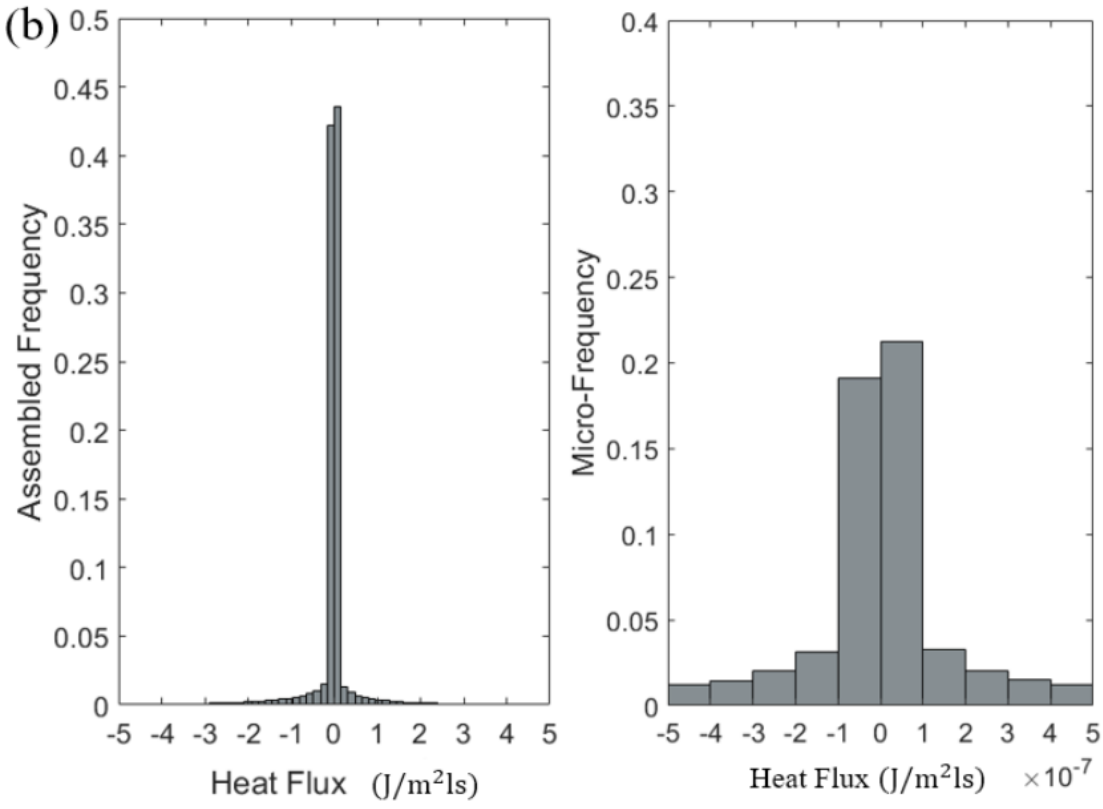

657

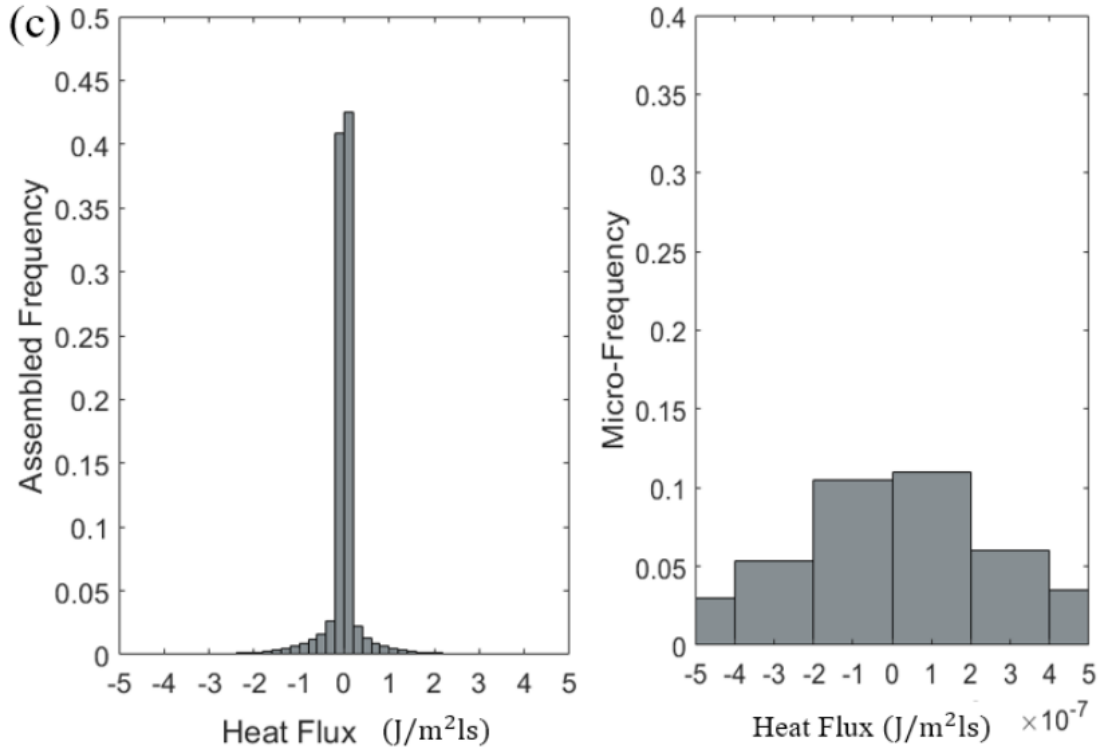

658

659 Fig. 14 Data *vi* Heat flux distribution in S group at (a)0 ls, (b)0.5×10^5 ls and (c) 10^5 ls

660 The above results demonstrate the microscopic complexity of the local heat conduction
661 in packed beds. Since the packing structure has been strictly defined with specific
662 image-based geometry, the mathematical description of the time-dependent spatial
663 distribution of heat flux becomes a statistical collection of the thermal status in each
664 coordinate. In comparison with the existing top-down approach to describe the overall

thermal status with a homogeneous assumption, the presented bottom-up approach demonstrated the ability to reproduce the local thermal behaviour and the integrated global thermal performance. Although the molecular-level structure has not been defined in this work, the positioning of the solid-air interface in the current framework can already provide algorithmic construction space to couple with smaller-scale analysis.

3.5 Endpoint output verification with previous experiments

The multiscale heat conduction in heterogeneous media involves the local heat flux distribution, heat transfer along the temperature gradient, temperature change over time and energy storage/release, after which the round-trip energy efficiency is calculated as an endpoint output in macroscale. For the convenience of real experimental measurement, measuring the multidirectional energy status at each mesoscopic coordinate over the whole conduction period is often impractical. This raises the necessity for the construction of the digital environment reflected by this work. The influence of the packing structure difference was extracted through the strict control of the same boundary conditions and initial conditions. As a result, the heat conduction performance with different packing structures can be compared in the same digital environment without noise interference from other types of heat and mass transfer. In addition to the algorithmic validation with theoretical and experimental studies from the beginning, endpoint verification is still necessary to ensure the process validity. The computation of energy round-trip efficiency has already involved the heat evolution over the heterogeneous space, making this dimensionless property highly suitable for cross-comparison with existing experiments. In this work, the energy round-trip efficiency tracking leads to a range of results from 63% to 91% for stable efficiency during energy storage and release. In previous experimental studies of packed bed energy systems, a similar results range has been observed, including 64% to 98% [9], 77% to 81% [75], 71%[76] and 59% to 71%[77]. Additionally, the experimental results in [78] not only reported a range of 78% to 95% but also recorded the early increment of the round-trip efficiency, similar to the behaviour of the digital conduction in this study. Although the materials of packed beds in this work and the above-mentioned studies are different, the energy round-trip efficiency eventually shares a high coverage of the range. This accordance indicates that the energy round-trip efficiency of a packed bed system is an intrinsic property of the packed structure, and the influence of the material composition is limited.

3.6 Current challenges and future perspective

The proposed framework presented a prototype to perform a heat conduction simulation in realistic structures reconstructed from 3D image data. The image-based input makes the framework compatible with the rapid development of image acquisition techniques. Although the feasibility has been demonstrated with the above verified outputs, it still faces limitations from both hardware and software. Since the core data in the mesoscopic simulation is the heat flux tensor at each coordinate, an indirect comparison becomes necessary during the calibration and validation. This necessity at the current time is a result of the lack of techniques to physically acquire the multi-directional heat flux over the porous space. On the other hand, the presented framework is one of the software solutions to obtain the instantaneous conduction distribution map throughout

digital or practical samples. Another limitation is that the personal computer at the current time still faces a lack of computing capability to perform extremely large or multiple simulations fully in the mesoscale. Fortunately, the overcoming of this limitation can already be discussed before the fundamental improvement of computational hardware. In future work, software improvements such as parallel computation will help the mesoscopic simulation to include sensitivity quantification with numerous inputs. Although the current inputs with different porous media can already illustrate the influence of geometrical uncertainty to some extent, the impurity of material in packed beds in practice also leads to a variation of their thermal performance. Hence, another important development in the future would be the stochastic distribution of different material properties over the porous space. The above perspective presents an establishment of a digital understanding of the still complicated phenomenon, having the potential to provide an images-to-results routine for specific engineering practice.

4.0 Conclusion

In this work, we developed a computational framework to model the heat conduction in packed beds with heterogeneity. The pre-processing adopted an original random packing with realistic rock data. The core computation applied an original D3Q7 lattice-based partial differential equation solver, presenting an algorithmic innovation of expanding the original density computation in microscale to heat transfer computation in mesoscale. The post-processing introduced several digital tests, including heat tracking, energy tracking, temperature tracking, round-trip efficiency and heat flux distribution. The anisotropic behaviour of heat conduction in heterogeneous media was digitally recovered with scaled analytical validation. This work provided a feasible approach to enrich the methodology options of the packed bed system in terms of analysis and design. The digital basis of the presented work identifies the standalone contribution towards the development of multiscale modelling on the thermal behaviour in packed beds. The main findings from the results are as follows:

(1) The increment of solid phase fraction is in favour of both heat storage and release. RCP for irregular particle packing is necessary for the thermal analysis in packed beds. The virtual device with natural rocks is capable of providing energy storage and release balance up to 55.6 lattice hours, during which the peak energy exchange rate occurs at around 27.8 lattice hours without other types of heat transfer. There exists a balanced line of particle-air interaction and boundary-environment interaction within 34.93% and 42.33% solid phase fractions. The exponential function can properly describe the heat exchange evolution, and the power function can properly recover the energy evolution.

(2) The packing structure with a higher solid phase fraction is less sensitive to the heating and cooling process. A suggestion to improve the temperature maintenance performance of an existing thermal device was deduced as filling the currently empty chamber with closely packed rocks. The energy efficiency can reach a high level after 27.8 lattice hours without external interference. Decrement of the solid phase fraction enhances the heat intake efficiency. The major amount of energy exchange has already occurred during the relatively low-efficiency stage. The critical time threshold for

beneficial round-trip efficiency is at around 13.89 lattice hours without additional thermal interference. Energy round-trip efficiency is an intrinsic property of the packed structure. The material of the packed bed only has a limited influence on the energy round-trip efficiency.

(3) It was found that the heat flux distribution is a composite of distributions of two scales. The generalised logistic function with different parameters can provide a fitting recovery of the heat flux distribution. The external boundary-environment interaction triggered decreased grading, and the internal particle-air interaction triggered increased grading of the heat flux. The investigation in this work demonstrates the feasibility of analysing heat transfer in heterogeneous media with the developed framework. A profound amount of methodological construction is still needed to construct the full map of the multiscale thermodynamics within packed beds.

Declaration of competing interest

The authors declare that they have no known competing financial interests or personal relationships that could have appeared to influence the work reported in this paper.

CRediT author statement

Mingzhi Wang: Conceptualization, Methodology, Software, Validation, Formal analysis, Investigation, Data curation, Writing - Original Draft, Writing - Review & Editing, Resources, Visualization, Supervision, Project administration, Funding acquisition. **Chaoyang Shang:** Conceptualization, Investigation, Funding acquisition. **Liang Li**： Funding acquisition, Project administration, Resources. **Xu Yang:** Investigation, Resources, Data curation, Formal analysis. **Wei Zhao**: Investigation, Formal analysis, Project administration. **Abir Al-Tabbaa:** Methodology, Resources, Supervision.

Data availability

Data will be made available on request.

Acknowledgement

The authors gratefully acknowledge the financial support provided by the Key Lab of Structures Dynamic Behavior and Control of the Ministry of Education, Harbin Institute of Technology (HITCE202401), Natural Science Foundation of Heilongjiang Province (No. YQ2024E029) and National Key R&D Program of China (2024YFC2816400)

References

[1] R. Zhang, Y. Wang, H. Ren, W. Li, Z. Tang, D. Zhang, Multi-scale study of turbulent mass transfer process in different shaped-adsorbent packed bed, Int. J. Heat Mass Transf. 218 (2024). doi:10.1016/j.ijheatmasstransfer.2023.124810.

[2] M. Fierro, C. Gutierrez, V. Jovicic, M. Toledo, Hollow spheres as inert packed bed from lean to rich combustion in porous media, Int. J. Heat Mass Transf. 195 (2022). doi:10.1016/j.ijheatmasstransfer.2022.123067.

[3] T. Shimada, H. Yamasaki, T. Kuroki, J. Kang, D.W. Kim, T. Yagi, M. Okubo,

Wet-Type Packed-Bed Nonthermal Plasma for Simultaneous Removal of PM and VOCs, Plasma Chem. Plasma Process. 44 (2024) 239–255. doi:10.1007/s11090-023-10403-1.

[4] M.K. Park, S.G. Ryu, H.B. Park, H.W. Lee, K.C. Hwang, C.H. Lee, Decomposition of cyanogen chloride by using a packed bed plasma reactor at dry and wet air in atmospheric pressure, Plasma Chem. Plasma Process. 24 (2004) 117–136. doi:10.1023/B:PCPP.0000004885.20686.ed.

[5] K. Muthaiyan, R. Narayanasamy, C. Lakshmanan, P. Vellaichamy, V. Ramalingam, Residential air conditioning system integrated with packed bed cool storage unit for promoting rooftop solar pv power generation, Int. J. Renew. Energy Dev. 10 (2021) 239–247. doi:10.14710/ijred.2021.33750.

[6] J. Liu, S. Lu, Thermal performance of packed-bed latent heat storage tank integrated with flat-plate collectors under intermittent loads of building heating, Energy. 299 (2024). doi:10.1016/j.energy.2024.131463.

[7] A. Gautam, R.P. Saini, Performance analysis and system parameters optimization of a packed bed solar thermal energy storage having spherical packing elements with pores, J. Energy Storage. 48 (2022). doi:10.1016/j.est.2022.103993.

[8] A.J. Hawkins, J.T. Bender, R.D. Grooms, C.J. Schissel, J.W. Tester, Temperature-responsive smart tracers for field-measurement of inter-well thermal evolution: Heterogeneous kinetics and field demonstration, Geothermics. 92 (2021). doi:10.1016/j.geothermics.2021.102046.

[9] X. She, X. Wang, P. Han, Y. Li, C. Wang, Enhancement of efficiencies of cryogenic energy storage packed bed using a novel Referred-Standard-Volume optimization method, Int. J. Heat Mass Transf. 224 (2024). doi:10.1016/j.ijheatmasstransfer.2024.125367.

[10] Y. Guan, J. Yan, Y. Shan, Y. Zhou, Y. Hang, R. Li, Y. Liu, B. Liu, Q. Nie, B. Bruckner, K. Feng, K. Hubacek, Burden of the global energy price crisis on households, Nat. Energy. 8 (2023) 304–316. doi:10.1038/s41560-023-01209-8.

[11] H.F. Goessling, T. Rackow, T. Jung, Recent global temperature surge intensified by record-low planetary albedo, Science. 387 (2025) 68–73. doi:10.1126/science.adq7280.

[12] M. Abedi, X. Tan, P. Saha, J.F. Klausner, A. Bénard, Design of a solar air heater for a direct-contact packed-bed humidification–dehumidification desalination system, Appl. Therm. Eng. 244 (2024). doi:10.1016/j.applthermaleng.2024.122700.

[13] S. Zhang, Z. Wen, X. Liu, X. Liu, S. Wang, H. Zhang, Experimental study on the permeability and resistance characteristics in the packed bed with the multi-size irregular particle applied in the sinter vertical waste heat recovery technology, Powder Technol. 384 (2021) 304–312. doi:10.1016/j.powtec.2021.02.027.

[14] H. Geng, Y. Wu, D. Ma, Y. Hao, D. Li, H. Zhou, Experimental study on the heat storage characteristics of rock bed heat storage system with different packing structure, J. Energy Storage. 101 (2024). doi:10.1016/j.est.2024.113973.

[15] A. Soria-Verdugo, J.F. Guil-Pedrosa, F. Hernández-Jiménez, L.M. García-Gutiérrez, E. Cano-Pleite, N. García-Hernando, Experimental analysis of a novel confined bed system for thermal energy storage, J. Energy Storage. 69 (2023) 107972. doi:10.1016/j.est.2023.107972.

[16] K. Furuichi, K. Katayama, H. Date, T. Takeishi, S. Fukada, Tritium sorption behavior on the percolation of tritiated water into a soil packed bed, Fusion Eng. Des. 109–111 (2016) 1371–1375. doi:10.1016/j.fusengdes.2015.12.019.

[17] A.S. Pereira, R.M. da Silva, R.S. Santos, A.G.B. de Lima, R.O. de Andrade, W.M.P.B. de Lima, G.S. de Lima, Heat Transfer in a Packed-Bed Elliptic Cylindrical Reactor: Theory, Heterogeneous Transient Modeling, and Applications, Adv. Struct. Mater. 133 (2021) 185–214. doi:10.1007/978-3-030-47856-8_7.

[18] M. Khaljani, M. Nazari, M. Azarpeyvand, Y. Mahmoudi, Experimental and Pore-Scale Analysis of Flow and Thermal Fields in a Packed Bed Channel, Heat Transf. Eng. 43 (2022) 1119–1134. doi:10.1080/01457632.2021.1943846.

[19] L.N. Smith, P.S. Midha, Computer simulation of morphology and packing behaviour of irregular particles, for predicting apparent powder densities, Comput. Mater. Sci. 7 (1997) 377–383. doi:10.1016/S0927-0256(97)00003-7.

[20] A. Donev, S. Torquato, F.H. Stillinger, R. Connelly, Jamming in hard sphere and disk packings, J. Appl. Phys. 95 (2004) 989–999. doi:10.1063/1.1633647.

[21] C.S. O'Hern, S.A. Langer, A.J. Liu, S.R. Nagel, Random packings of frictionless particles, Phys. Rev. Lett. 88 (2002) 755071–755074. doi:10.1103/physrevlett.88.075507.

[22] a.B. Yu, L.F. Liu, Z.P. Zhang, R.Y. Yang, R.P. Zou, Computer simulation of the packing of fine particles, Int. J. Mater. Prod. Technol. 19 (2003) 324. doi:10.1504/IJMPT.2003.002516.

[23] R. Ni, M.A.C. Stuart, M. Dijkstra, Pushing the glass transition towards random close packing using self-propelled hard spheres, Nat. Commun. 4 (2013). doi:10.1038/ncomms3704.

[24] M. Kozejova, R. Bodnarova, V. Latyshev, M. Lisnichuk, V. Girman, H. You, V. Komanicky, Structural dependence of hydrogen evolution reaction on transition metal catalysts sputtered at different temperatures in alkaline media, Int. J. Hydrogen Energy. 47 (2022) 26987–26999. doi:10.1016/j.ijhydene.2022.06.036.

[25] J. Zhang, Y. Zhu, T. Ragab, W. Wang, H. Zhang, X. Wang, K. Jiang, Numerical modeling of Van der Waals interaction between a spherical particle and rough surfaces with different planar asperity distributions, Powder Technol. 428 (2023). doi:10.1016/j.powtec.2023.118877.

[26] V. Baranau, U. Tallarek, Estimating angoricity and granular equations of state for monodisperse packings of frictional hard spheres in a wide range of densities, Phys. Rev. E. 109 (2024). doi:10.1103/PhysRevE.109.044904.

[27] G.Y. Onoda, E.G. Liniger, Random loose packings of uniform spheres and the dilatancy onset, Phys. Rev. Lett. 64 (1990) 2727–2730. doi:10.1103/PhysRevLett.64.2727.

881 [28] V. Baranau, S.C. Zhao, M. Scheel, U. Tallarek, M. Schröter, Upper bound on the
882 Edwards entropy in frictional monodisperse hard-sphere packings, Soft Matter.
883 12 (2016) 3991–4006. doi:10.1039/c6sm00567e.

884 [29] P.K. Ghorai, S. Yashonath, The stokes - Einstein relationship and the levitation
885 effect: Size-dependent diffusion maximum in dense fluids and close-packed
886 disordered solids, J. Phys. Chem. B. 109 (2005) 5824–5835.
887 doi:10.1021/jp046312w.

888 [30] P. Viot, G. Tarjus, Random Sequential Addition of Unoriented Squares:
889 Breakdown of Swendsen's Conjecture, Europhys. Lett. 13 (1990) 295–300.
890 doi:10.1209/0295-5075/13/4/002.

891 [31] G. Tarjus, P. Schaaf, J. Talbot, Random sequential addition: A distribution
892 function approach, J. Stat. Phys. 63 (1991) 167–202. doi:10.1007/BF01026598.

893 [32] G. Zhang, S. Torquato, Precise algorithm to generate random sequential addition
894 of hard hyperspheres at saturation, Phys. Rev. E - Stat. Nonlinear, Soft Matter
895 Phys. 88 (2013). doi:10.1103/PhysRevE.88.053312.

896 [33] B. Lubachevsky, F. Stillinger, Geometric Properties of Ran- dom Disk Packings,
897 J. Stat. Phys. 60 (1990) 561–583.

898 [34] C.S. Chang, L. Ma, A micromechanical-based micropolar theory for deformation
899 of granular solids, Int. J. Solids Struct. 28 (1991) 67–86. doi:10.1016/0020-
900 7683(91)90048-K.

901 [35] M. Moody, J.R. Ray, A. Rahman, Close-packed (polytypic) structures in
902 molecular-dynamics simulations, Phys. Rev. B. 35 (1987) 557–570.
903 doi:10.1103/PhysRevB.35.557.

904 [36] A. Donev, I. Cisse, D. Sachs, E.A. Variano, F.H. Stillinger, R. Connelly, S.
905 Torquato, P.M. Chaikin, Improving the Density of Jammed Disordered Packings
906 Using Ellipsoids, Science (80-.). 303 (2004) 990–993.
907 doi:10.1126/science.1093010.

908 [37] L. Xu, X. Wu, S. Wang, S. Bao, Multi-level coarse-grained discrete element
909 method modeling of cylinder particle flow in a rotating drum, Particuology. 88
910 (2024) 218–238. doi:10.1016/j.partic.2023.09.015.

911 [38] K. Wu, W. Sun, S. Liu, G. Cai, Influence of particle shape on the shear behavior
912 of superellipsoids by discrete element method in 3D, Adv. Powder Technol. 32
913 (2021) 4017–4029. doi:10.1016/j.apt.2021.09.001.

914 [39] Y. Jang, E. Kim, J. Yang, J. Rho, Physics-informed discrete element modeling
915 for the bandgap engineering of cylinder chains, Appl. Math. Model. 125 (2024)
916 571–590. doi:10.1016/j.apm.2023.09.011.

917 [40] Z. Shen, D. Huang, G. Wang, Y. Zhao, F. Jin, A mesoscale bond model for
918 discrete element modeling of irregular cemented granular materials, Comput.
919 Geotech. 152 (2022). doi:10.1016/j.compgeo.2022.105051.

920 [41] W. Xu, B. Zhang, M. Jia, W. Wang, Z. Gong, J. Jiang, Discrete element
921 modeling of 3D irregular concave particles: Transport properties of particle-
922 reinforced composites considering particles and soft interphase effects, Comput.
923 Methods Appl. Mech. Eng. 394 (2022). doi:10.1016/j.cma.2022.114932.

924 [42] X. Jia, R.. Williams, A packing algorithm for particles of arbitrary shapes,
925 Powder Technol. 120 (2001) 175–186. doi:10.1016/S0032-5910(01)00268-6.

926 [43] M. Wang, A. Al-Tabbaa, W. Wang, Improving discrete particle packing models
927 for the microstructural formation simulation of Portland cement, Constr. Build.
928 Mater. 229 (2019). doi:10.1016/j.conbuildmat.2019.116841.

929 [44] M. Wang, X. Yang, W. Wang, Establishing a 3D aggregates database from X-
930 ray CT scans of bulk concrete, Constr. Build. Mater. 315 (2022) 125740.
931 doi:10.1016/j.conbuildmat.2021.125740.

932 [45] R. Kovács, Heat equations beyond Fourier: From heat waves to thermal
933 metamaterials, Phys. Rep. 1048 (2024) 1–75.
934 doi:10.1016/j.physrep.2023.11.001.

935 [46] R. Kovács, P. Rogolino, Numerical treatment of nonlinear Fourier and Maxwell-
936 Cattaneo-Vernotte heat transport equations, Int. J. Heat Mass Transf. 150 (2020).
937 doi:10.1016/j.ijheatmasstransfer.2019.119281.

938 [47] A. Ahmad, J.S. Saini, H.K. Varma, Effect of geometrical and thermophysical
939 characteristics of bed materials on the enhancement of thermal performance of
940 packed bed solar air heaters, Energy Convers. Manag. 36 (1995) 1185–1195.
941 doi:10.1016/0196-8904(95)00006-Y.

942 [48] Y. Qu, L. Wang, X. Lin, H. Ling, Y. Bai, S. Zhang, H. Chen, Heat transfer
943 characteristics of mixed convection in packed beds, Chem. Eng. Sci. 255 (2022)
944 117679. doi:10.1016/j.ces.2022.117679.

945 [49] L. Pimienta, N. Klitzsch, C. Clauser, Comparison of thermal and elastic
946 properties of sandstones: Experiments and theoretical insights, Geothermics. 76
947 (2018) 60–73. doi:10.1016/j.geothermics.2018.06.005.

948 [50] Z. Zhou, J. Zhang, Z. Li, X. Li, H. Yang, Computational model for the thermal
949 conductivity of soil-rock mixture, Int. J. Heat Mass Transf. 230 (2024).
950 doi:10.1016/j.ijheatmasstransfer.2024.125745.

951 [51] A. Zenner, K. Fiaty, V. Bellière-Baca, C. Rocha, G. Gauthier, D. Edouard,
952 Effective heat transfers in packed bed: Experimental and model investigation,
953 Chem. Eng. Sci. 201 (2019) 424–436. doi:10.1016/j.ces.2019.02.028.

954 [52] Y.K. Recepoğlu, N. Kabay, I.Y. Ipek, M. Arda, M. Yüksel, K. Yoshizuka, S.
955 Nishihama, Packed bed column dynamic study for boron removal from
956 geothermal brine by a chelating fiber and breakthrough curve analysis by using
957 mathematical models, Desalination. 437 (2018) 1–6.
958 doi:10.1016/j.desal.2018.02.022.

959 [53] T.R.G. Davenne, S.D. Garvey, B. Cardenas, J.P. Rouse, Stability of packed bed
960 thermoclines, J. Energy Storage. 19 (2018) 192–200.
961 doi:10.1016/j.est.2018.07.015.

962 [54] M. Kandula, On the effective thermal conductivity of porous packed beds with
963 uniform spherical particles, J. Porous Media. 14 (2011) 919–926.
964 doi:10.1615/JPorMedia.v14.i10.70.

965 [55] Q. Liao, Y.X. Yang, X. Zhu, R. Chen, Q. Fu, A simulation on flow and mass
966 transfer in a packed bed photobioreactor for hydrogen production, Int. J. Heat

Mass Transf. 109 (2017) 1132–1142. doi:10.1016/j.ijheatmasstransfer.2017.02.084.

[56] N. Zobel, F. Behrendt, Transient heat transfer in packed beds: The significance of the history term, Int. J. Heat Mass Transf. 51 (2008) 3816–3824. doi:10.1016/j.ijheatmasstransfer.2007.10.040.

[57] J.I. Córcoles, M. Díaz-Heras, P. Domínguez Coy, J.A. Almendros-Ibáñez, 3-D numerical simulation of the heat transfer of a fluidized bed with a horizontal tube bundle and Geldart D particles, Int. J. Heat Mass Transf. 225 (2024). doi:10.1016/j.ijheatmasstransfer.2024.125406.

[58] L.C. Cheng, S.C. Wong, A new LTNE analysis process for predicting the steady-state temperature distribution in a fixed bed of randomly packed mono-sized rough spheres based on pore-scale simulations, Int. J. Heat Mass Transf. 221 (2024). doi:10.1016/j.ijheatmasstransfer.2023.125036.

[59] M. Wang, S. Bu, B. Zhou, B. Gong, Z. Li, D. Chen, Pore-scale simulation on flow and heat transfer characteristics in packed beds with internal heat sources at low Reynolds numbers, Int. J. Heat Mass Transf. 213 (2023). doi:10.1016/j.ijheatmasstransfer.2023.124325.

[60] N. Sassine, F.V. Donzé, B. Harthong, A. Bruch, Thermal stress numerical study in granular packed bed storage tank, Granul. Matter. 20 (2018). doi:10.1007/s10035-018-0817-y.

[61] E. Noël, D. Teixeira, G. Preux, Modelling of gas-solid heat transfer and pressure drop in a rock-packed bed using pore-scale simulations, Int. J. Heat Mass Transf. 214 (2023) 124432. doi:10.1016/j.ijheatmasstransfer.2023.124432.

[62] X. Jia, N. Gopinathan, R. a. Williams, Modeling complex packing structures and their thermal properties, Adv. Powder Technol. 13 (2002) 55–71. doi:10.1163/15685520252900956.

[63] G. Dalla Santa, A. Galgaro, R. Sassi, M. Cultrera, P. Scotton, J. Mueller, D. Bertermann, D. Mendrinos, R. Pasquali, R. Perego, S. Pera, E. Di Sipio, G. Cassiani, M. De Carli, A. Bernardi, An updated ground thermal properties database for GSHP applications, Geothermics. 85 (2020). doi:10.1016/j.geothermics.2019.101758.

[64] M. Soltani, F. Moradi Kashkooli, M. Souri, B. Rafiei, M. Jabarifar, K. Gharali, J.S. Nathwani, Environmental, economic, and social impacts of geothermal energy systems, Renew. Sustain. Energy Rev. 140 (2021). doi:10.1016/j.rser.2021.110750.

[65] S. Inac, S.O. Unverdi, A. Midilli, Global warming, environmental and sustainability aspects of a geothermal energy based biodigester integrated SOFC system, Int. J. Hydrogen Energy. 45 (2020) 35039–35052. doi:10.1016/j.ijhydene.2020.06.224.

[66] I. Calderón-Vásquez, E. Cortés, J. García, V. Segovia, A. Caroca, C. Sarmiento, R. Barraza, J.M. Cardemil, Review on modeling approaches for packed-bed thermal storage systems, Renew. Sustain. Energy Rev. 143 (2021). doi:10.1016/j.rser.2021.110902.

[67] D. Ji, C. Li, C. Zhai, Z. Cao, An Efficient Platform for Numerical Modeling of Partial Differential Equations, IEEE Trans. Geosci. Remote Sens. 62 (2024). doi:10.1109/TGRS.2024.3409620.

[68] J.W. Eaton, GNU Octave and reproducible research, J. Process Control. 22 (2012) 1433–1438. doi:10.1016/j.jprocont.2012.04.006.

[69] Material Properties, Common Materials, (2025). https://material-properties.org (accessed April 10, 2025).

[70] S.N. Emirov, A.A. Aliverdiev, Y.P. Zarichnyak, R.M. Emirov, Studies of the Effective Thermal Conductivity of Sandstone Under High Pressure and Temperature, Rock Mech. Rock Eng. 54 (2021) 3165–3174. doi:10.1007/s00603-020-02353-3.

[71] D. Koňáková, E. Vejmelková, R. Černý, Thermal properties of selected sandstones, Adv. Mater. Res. 982 (2014) 100–103.

[72] Hrifech S., Bennouna E, Faik A., Mouguina E. M, Mimet A., Experimental assessment of quartz-rich rocks as storage materials for medium and high temperatures air packed bed system, J. Energy Storage. (2023).

[73] M. Hamidi, V.M. Wheeler, P. Kreider, K. Catchpole, A.W. Weimer, Effective thermal conductivity of a bed packed with granular iron–manganese oxide for thermochemical energy storage, Chem. Eng. Sci. 207 (2019) 490–494. doi:10.1016/j.ces.2019.06.035.

[74] M. Wang, Y. Liu, B. Qi, A. Al-Tabbaa, W. Wang, Percolation and conductivity development of the rod networks within randomly packed porous media, Compos. Part B Eng. 187 (2020) 107837. doi:10.1016/j.compositesb.2020.107837.

[75] Y. Jemmal, N. Zari, M. Asbik, M. Maaroufi, Experimental characterization and thermal performance comparison of six Moroccan rocks used as filler materials in a packed bed storage system, J. Energy Storage. 30 (2020). doi:10.1016/j.est.2020.101513.

[76] C.H. Fan, M.J. Li, M.J. Li, L.J. Chen, Z. Bin Liu, Performance analysis and optimization of an adiabatic compressed air energy storage system coupled with the packed-bed thermal energy storage device, Energy. 324 (2025). doi:10.1016/j.energy.2025.135939.

[77] W.H. Gerstle, N.R. Schroeder, L.P. McLaughlin, C.K. Ho, H.F. Laubscher, S. Kao, Experimental testing and computational modeling of a radial packed bed for thermal energy storage, Sol. Energy. 264 (2023). doi:10.1016/j.solener.2023.111993.

[78] I. Calderón-Vásquez, J.M. Cardemil, A comparison of packed-bed flow topologies for high-temperature thermal energy storage under constrained conditions, Appl. Therm. Eng. 238 (2024). doi:10.1016/j.applthermaleng.2023.121934.